

# Impact of changing concavity indices on channel steepness and divide migration metrics

Boris Gailleton<sup>1</sup>, Simon M. Mudd<sup>1</sup>, Fiona J. Clubb<sup>2</sup>, Stuart W.D. Grieve<sup>3,4</sup>,  
and Martin D. Hurst<sup>5</sup>

<sup>1</sup>School of GeoSciences, University of Edinburgh, UK <sup>2</sup>Department of Geography, Durham University, UK <sup>3</sup>School of Geography, Queen Mary University of London, UK <sup>4</sup>Digital Environment Research Institute, Queen Mary University of London, UK <sup>5</sup>School of Geographical & Earth Sciences, University of Glasgow, UK

## Key Points:

- We develop metrics to explore the variability of the concavity index in a given landscape, and assess its suitability for a given landscape
- We compute the values of concavity index ( $\theta$ ) in basins across the globe (N=5033). The central tendency is 0.425, corroborating previous studies, but there is a large range in values, with interquartile range of 0.225–0.575.
- We find that the channel steepness index ( $k_{sn}$ ), the  $\chi$  coordinate and knickpoint extraction are all sensitive to the value of  $\theta_{ref}$ , with implications for river profile analysis and the detection of migrating drainage divides in landscapes with variable concavities.

---

Corresponding author: Boris Gailleton, School of GeoSciences, University of Edinburgh, Drummond Street, Edinburgh, EH8 9XP, UK, [s1675537@sms.ed.ac.uk](mailto:s1675537@sms.ed.ac.uk)

## Abstract

The concavity index,  $\theta$ , describes how quickly river channel gradient declines downstream. It is used in calculations of normalized channel steepness index,  $k_{sn}$ , a metric for comparing the relative steepness of channels with different drainage area. It is also used in calculating a transformed longitudinal coordinate,  $\chi$ , which has been employed to search for migrating drainage divides. A  $\theta$  value of 0.45 is typically assumed in studies. Here we quantify the variability in  $\theta$  across multiple landscapes distributed across the globe. We describe the degree to which both the spatial distribution and magnitude of  $k_{sn}$  and  $\chi$  can be distorted if  $\theta$  is assumed rather than constrained. Differences between constrained and assumed  $\theta$  of 0.1 or less are unlikely to affect the spatial distribution and relative magnitude of  $k_{sn}$  values, but larger differences can change the spatial distribution of  $k_{sn}$  and in extreme cases invert differences in relative steepness: relatively steep reaches can appear relatively gentle as quantified by  $k_{sn}$ . These inversions are function of the range of drainage area in the considered watersheds. We also demonstrate that the  $\chi$  coordinate, and therefore the detection of migrating drainage divides, is sensitive to varying values of  $\theta$ . The median of most likely  $\theta$  across a wide range of mountainous and upland environments is 0.425. This wide range of variability suggests workers should not assume any value for  $\theta$ , but should instead calculate a representative  $\theta$  for the landscape of interest, and exclude basins for which this value is a poor fit.

## Plain Language Summary

The elevation profiles of rivers are commonly used to interpret their tectonic and erosion history. The slope of river channels tends to decline downstream, and this decline can be described by a river's concavity. Estimating the concavity is important when comparing river profiles across a region, and using an assumed value for concavity may result in spurious interpretations.

## 1 Introduction

For over a century, geoscientists have recognised the potential of fluvial geomorphology to unravel links between landscape evolution and external forcing (e.g. Gilbert, 1880; Davis, 1899). In his review of physical geography at the time, de Lapparent (1896) outlined a number of basic observations underpinning modern geomorphology: the systematic concave up shape of river long profiles, the hypothesis that erosion is correlated with channel gradient, and that lithologic contrasts and inherited tectonic structures influence river profile form. The geometry of river profiles later became one of the key tools for geoscientists in the first half of the 20<sup>th</sup> century for interpreting landscapes (e.g. Knopf, 1924).

Assuming that channel gradient encodes information about erosion rates, lithology, or other factors, one is faced with a fundamental problem: the concave nature of a typical river prohibits comparison of gradients between river reaches with different drainage areas. That is, how can one tell if a headwater channel is steeper than a section of the river some distance downstream in a way that is meaningful for interpreting landscape evolution? Some normalization is required to compare river sections with different drainage areas.

Morisawa (1962) noted a power law relationship between gradient and drainage area, which led to a means of normalizing river gradients. Flint (1974) formalized these observations into the slope–area relationship with a concavity index ( $\theta$ ), which describes how quickly river gradient decreases with increasing drainage area, and a steepness index ( $k_s$ ) that describes the relative steepness of a reach regardless of its drainage area:

$$S = k_s A^{-\theta} \quad (1)$$

where  $S$  is the gradient of elevation along the channel ( $S = dz/dx$  where  $z$  is the elevation and  $x$  the flow distance); and  $A$  is the drainage area. This relative steepness index  $k_s$ , in particular, has been widely used in geomorphology because of its empirically observed positive correlation with erosion rates (e.g., Safran et al., 2005; DiBiase et al., 2010; Cyr et al., 2010; Scherler et al., 2014; Ouimet et al., 2009; Kirby & Whipple, 2012; Mandal et al., 2015; Harel et al., 2016), supported by a theoretical underpinning (Whipple & Tucker, 1999). Note that it has been commonly suggested that this relationship mostly applies above a critical drainage area representing the switch from domains dominated by debris-flows to those dominated by fluvial incision (Whipple et al., 2013, and references therein).

Equation 1 can be rearranged so that  $k_s$  can be calculated at any point in a drainage network given the local values of  $S$  and  $A$ . This value depends on the value of the concavity index. In addition the units of  $k_s$  depend on  $\theta$  (they are  $m^{2\theta}$ ). Drainage areas within channel networks can vary over several orders of magnitude so changing the exponent of  $A$  in equation 1 has a large effect on  $k_s$  if it is used to calculate  $k_s$  values. For example, for a hypothetical location where  $S = 0.05$  and  $A = 1e8 \text{ m}^2$ ,  $k_s = 12.56 \text{ m}^{0.6}$  if  $\theta = 0.3$  whereas  $k_s = 3155 \text{ m}^{1.2}$  if  $\theta = 0.6$ .

In order to compare  $k_s$  within different channels, the steepness index is typically calculated with a fixed value of  $\theta$ . This is called the reference concavity index, denoted by  $\theta_{ref}$ . When a reference concavity index is used, the resulting value of the channel steepness index is called “normalized” and is denoted with the symbol  $k_{sn}$  with fixed units (Wobus et al., 2006).

Despite the importance of constraining  $\theta$  for calculating the channel steepness index, it is often assumed that  $0.4 < \theta < 0.6$  (e.g. Tucker & Whipple, 2002; Whipple, 2004; Kirby & Whipple, 2012). To illustrate the difference in magnitude and pattern of  $k_{sn}$  across different (but common)  $\theta_{ref}$  units, Figure 1 shows populations of  $k_{sn}$  in the same watershed for  $\theta_{ref} = 0.3$ ,  $\theta_{ref} = 0.45$  and  $\theta_{ref} = 0.6$ .

For the rest of this study, we will use three terms to refer to concavity indices. We use  $\theta$  to generically refer to the concavity index, which can vary from a point to another. We use  $\theta_{opt}$  to refer to the best-fit  $\theta$  value for a particular region of interest, for example for a river catchment. Finally, we use  $\theta_{ref}$  to refer to a fixed value of  $\theta$  that is used to calculate  $k_{sn}$  or  $\chi$  over multiple catchments.

When extracting  $k_{sn}$  values, workers must, by definition, select  $\theta_{ref}$ , so what value should be used? Numerous theories exist to explain both bedrock and alluvial channel geometry. For example, if one assumes bedrock channel incision is proportional to shear stress, then the concavity index should be equal to  $\sim 0.43$  (e.g. Howard et al., 1994; Tucker & Whipple, 2002), whereas if bedrock channel incision is proportional to stream power per unit bed area then the concavity index should be equal to 0.5 (e.g. Whipple & Tucker, 1999). Since the 90s, many authors have introduced far more complex models of bedrock channel incision that account for sediment flux (e.g. Sklar & Dietrich, 1998; Gasparini et al., 2006), incision thresholds (e.g. DiBiase & Whipple, 2011; Lague et al., 2005), model individual processes such as abrasion and plucking (e.g. Chatanantavet & Parker, 2009) as well as models for channel profile evolution in alluvial rivers (e.g. Wickert & Schildgen, 2019). These models predict a range of concavity index values based on the tectonic, climatic, and sedimentary context. For example, Wickert and Schildgen (2019) predict that in gravel bed rivers, subsidence and uplift modulate the concavity index, with lower values of  $\theta$  when sediment flux is low or tectonic uplift is high. A recent model proposed by Turowski (2021) suggests that when the bedload fraction is independent of drainage area, concavity index values can range widely, with values ranging from 0.25 to 0.625 for

choices of bedload transport equations and channel width scaling that have been observed in nature. We would argue that there is no consensus as to the correct model, and even if you believed one of the above models were correct, unless direct observations of incision process, sediment flux, uplift and other factors were available it would be a challenge to calculate the concavity index based on parameterising a model.

Given the uncertainty in the appropriate value of  $\theta_{ref}$  for calculating  $K_{sn}$ , it is often assumed that  $0.4 < \theta < 0.6$  (e.g. Tucker & Whipple, 2002; Whipple, 2004; Kirby & Whipple, 2012), in some cases based on topographic observations (which we describe below) and in others invoking one of the models predicting channel geometry. Regardless of the way an author selects the value of  $\theta_{ref}$ , the selection can have a large impact on the values of  $k_{sn}$ , as illustrated by Figure 1. This shows populations of  $k_{sn}$  in the same watershed for  $\theta_{ref} = 0.3$ ,  $\theta_{ref} = 0.45$  and  $\theta_{ref} = 0.6$  and demonstrates both changes in magnitude and spatial pattern induced by different  $\theta_{ref}$ . As discussed in Gailleton et al. (2021), the large eastward drop of  $k_{sn}$  by values between 470 and 480 is linked to a combination of differential lithology and recent tectonics. However, the relative magnitude of this reduction depends on the choice of  $\theta_{ref}$ .

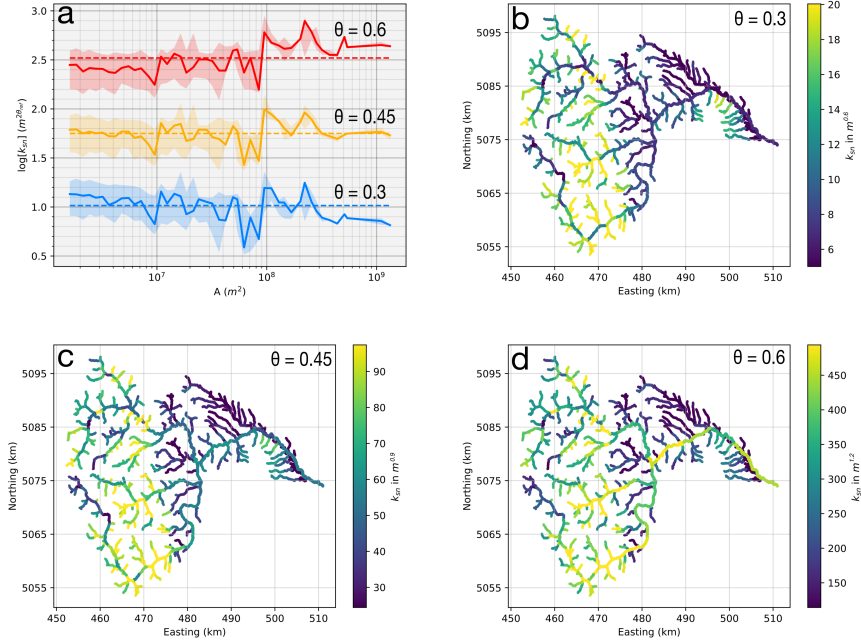


**Figure 1.** a) Example of populations of  $k_{sn}$  calculated for three different  $\theta_{ref}$  values as a function of drainage area. The watershed is the Putna river in Romania, 3000  $km^2$ , with outlet coordinates at 45.89 degrees latitude and 27.00 degrees longitude in WGS84. The solid line represents the median  $k_{sn}$  calculated with each value of  $\theta_{ref}$  and binned by drainage area in log space. The shaded area is the corresponding inter-quartile range. Note that the distribution of  $k_{sn}$  compared to the median varies depending on  $\theta_{ref}$ . For example, at low drainage areas,  $k_{sn}$  is above the mean for  $\theta_{ref} = 0.3$ , but below the mean for  $\theta_{ref} = 0.6$ . The solid line represents the median  $k_{sn}$  value over the whole area. b) c) and d): maps of  $k_{sn}$  values corresponding to a), respectively for  $\theta_{ref}$  equal to 0.3, 0.45 and 0.6. The spatial pattern differs depending on  $\theta_{ref}$ . To allow intercomparison between  $k_{sn}$  values with different magnitude and units, we set the minimum and maximum values of the color bars to the 10<sup>th</sup> and 90<sup>th</sup> quartile for each population.



We may be uncertain about the correct incision rule, and will therefore struggle to define a value of  $\theta_{ref}$  based on the physics of incision or sediment transport. We can, however, directly observe the concavity index using topographic data, as defined by equation 1. This has been attempted by numerous authors. For example, Tucker and Whipple (2002) compiled concavity indices using slope–area regression from ten previous studies, aggregating 27 different sites, and found concavity indices ranging from 0.11–1.13. Whipple (2004) argued that if you limit extraction of the concavity index to bedrock rivers with homogeneous substrates, homogeneous uplift fields and time invariant uplift, concavity indices converge to a range between 0.4–0.7.

Whipple (2004) went on to articulate circumstances in which concavity indices may fall outside this range. They argued that low concavity indices ( $\theta < 0.4$ ) can result from drainage basins influenced by debris flows (e.g. Stock & Dietrich, 2003) or from downstream increases in incision rate or rock strength (Kirby & Whipple, 2001). Alluvial rivers can also have low concavity values: Gasparini et al. (2004) used a numerical model to predict that finer sediment could result in low concavity values ( $< 0.4$ ) when either grain size was less than 100 mm in homogeneous sediment or if there was a high percentage of sand in mixed gravel and sand rivers. Whipple (2004) suggested that high concavities ( $\theta > 0.7$ ) could result from downstream transitions to full alluvial conditions with bedrock reaches in headwaters, and also noted the findings of Kirby and Whipple (2001) that high concavity can result from downstream increases in rock strength or incision rate. Extreme concavity values ( $\theta > 1.0$ ) can also result from large knickpoints (e.g. Schoenbohm et al., 2004). Furthermore, Zaprowski et al. (2005) found that channel concavities varied systematically across a gradient in mean annual precipitation and precipitation intensity, with higher concavities associated with a more intense hydrological settings on the high plains of the western USA.

Given the range of possible values of  $\theta$  both observed from topographic data and suggested by models, we wish to answer several questions. If one’s motivation is to use  $k_{sn}$  to compare channel profiles for the purpose of inferring erosion rates or tectonic uplift, does the choice of  $\theta_{ref}$  matter? If different basins have different values of the “correct” concavity index ( $\theta_{opt}$ ) does it matter to our interpretations if we apply the same  $\theta_{ref}$  to these basins? To do this, we attempt to constrain the range of concavity indices present both within and between a wide range of different study sites. We compare different methods of estimating the most likely values of  $\theta_{opt}$  and refine existing methods of quantifying the uncertainty in choosing a most likely value of  $\theta_{ref}$ . We then examine the impact of using a poorly-constrained reference concavity value on estimates of  $k_{sn}$  and the related metric  $\chi$ , which integrates drainage area along channels and has been used to detect drainage divide migration (Willett et al., 2014). We highlight the potential risks of misinterpretation in such cases, and also identify cases where a blanket value of  $\theta_{ref}$  can be applied across a landscape, despite spatially varying  $\theta_{opt}$ , without risk to interpretation of  $k_{sn}$  values.

## 2 Determining the concavity index

### 2.1 Concavity index derived from slope–area data

A common approach to deriving fluvial profile concavity is to transform equation 1 into logarithmic space:

$$\log[S] = \log[k_s] - \theta \log[A] \quad (2)$$

where  $\theta$  is the gradient of  $\log[A]$ – $\log[S]$  plots and  $k_s$  the intercept where  $\log[A] = 0$  (i.e., where  $A = 1 \text{ m}^2$  if areas are reported in square meters). Assuming  $k_s$  is a constant,  $\theta$  can be determined by linear regression of  $\log[A]$ – $\log[S]$ . This logarithmic slope–area method

has been widely used to determine both the concavity index and channel steepness index (e.g. Wobus et al., 2006; Kirby & Whipple, 2012; Whipple et al., 2013).

However, the use of raw  $S$ - $A$  data has limitations: the seminal Wobus et al. (2006) paper includes the word “pitfalls” in the title. DEM data is inherently noisy (e.g. Wobus et al., 2006; Perron & Royden, 2013), either because of natural noise in river profiles or due to errors in the acquisition methods (e.g. airborne lidar or satellite altimetry), and taking the gradient of noisy data amplifies that noise (e.g. Perron & Royden, 2013). In addition, tributaries result in large jumps in drainage area, resulting in major gaps along the  $\log[A]$  axis. Between tributaries, drainage area increases slowly, but channel gradient can vary dramatically due to heterogeneity in local river bed conditions. This means that some form of averaging or binning must be used on the raw slope–area data in order to extract  $k_s$  and  $\theta$  values.

We illustrate difficulties in extracting the concavity and steepness indices from  $S$ - $A$  in Figure 3. This figure contrasts a theoretical case (panel **a**) with real data that considers the basin as a whole (panel **b**), each different tributary channel individually (panel **c**), or solely the main stem channel (panel **d**). Values of  $\theta$  extracted from  $S$ - $A$  data can vary substantially in the same drainage basin depending on how this data is grouped and binned, as shown by the histograms of best-fit populations of  $\theta$  within the inset plots in panels **b,c,d**. This does not suggest that  $S$ - $A$  data is unsuitable for extracting landscape metrics: steepness indices derived from this method have been shown to correlate well with other landscape properties such as erosion rates and tectonic activity in a range of contexts (e.g. Kirby & Whipple, 2012). However it highlights the potential difficulties and uncertainties in using this technique to extract  $\theta$  or  $k_s$ , particularly across large areas where  $\theta$  might vary spatially.

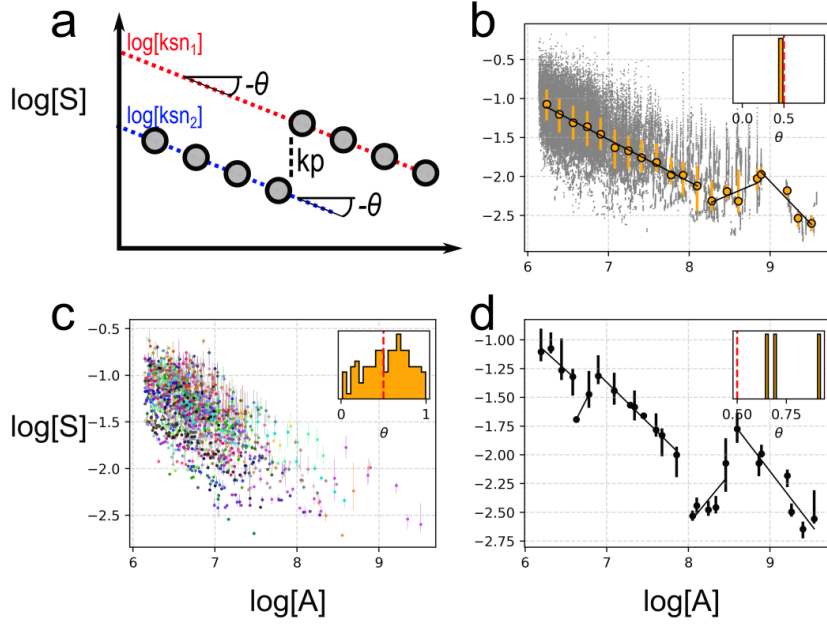


**Figure 2.** Example of different populations of  $\theta$  obtained from the same  $S$ – $A$  data using different grouping and binning. **a.** An idealized channel with slope and area following equation 1.  $\theta$  is uniform and a clear knickpoint separates two populations of  $k_s$ , or  $k_{sn}$  if  $\theta_{ref} = \theta$ . **b.** Slope–area data from a real watershed (the Buzău river in Romania, 3000 km<sup>2</sup>, with outlet coordinates at 45.20 degrees latitude and 26.75 degrees longitude in WGS84). Each grey point represents gradient calculated over a vertical window of 20 meters; data derived from the ALOS World 3D 30 dataset. Note the noise and irregularity of data spacing along the axes. In orange, data is binned by drainage area and concavity is calculated using a segmentation algorithm described in Mudd et al. (2014). Only one of the resulting segments has a concavity between 0 and 1: the inset in panels **b**, **c**, and **d** show histograms of concavity values between 0 and 1 based on segmentation of  $S$ – $A$  data. Panel **c.** shows slope–area data binned by drainage area for all tributaries of the same watershed. The population of  $\theta$  is obtained by using the segmentation of slope–area data in each each tributary. Panel **d.** shows data for the main stem channel only.

## 2.2 Concavity index from the integral approach

These problems with the slope–area approach have led to the development of alternative methods in recent years. One such technique is to integrate drainage area along flow distance, which was first suggested by Royden et al. (2000) and further developed in Perron and Royden (2013) as a way to circumvent uncertainties associated with calculating gradient from noisy topographic data. Following Whipple et al. (2017) we can integrate equation 1, resulting in

$$z(x) = z(x_b) + \left( \frac{k_s}{A_0^\theta} \right) \int_{x_b}^x \left( \frac{A_0}{A(x)} \right)^\theta dx, \quad (3)$$

where  $z(x_b)$  is the elevation of the channel at an arbitrary base level, and  $A_0$  is a reference drainage area, introduced to nondimensionalize the area term within the integral in equation (3). We can then define a longitudinal coordinate,  $\chi$ :

$$\chi = \int_{x_b}^x \left( \frac{A_0}{A(x)} \right)^{\theta} dx. \quad (4)$$

The coordinate  $\chi$  has dimensions of length, and is defined such that at any point in the channel:

$$z(x) = z(x_b) + \left( \frac{k_s}{A_0^{\theta}} \right) \chi. \quad (5)$$

Equation 5 has two key predictions: firstly, assuming that  $k_s$  and  $\theta$  are spatially constant (fixed to a  $\theta_{ref}$ ), there will be a linear relationship between  $\chi$  and elevation for a single channel; and secondly, that tributaries will be collinear with the main stem, i.e. both the main stem and its tributaries collapse on a line in  $\chi$  space. If the linearity prediction is true, a best-fitted  $\theta_{opt}$  can be calculated for a river by iterating through a range of  $\theta_{ref}$  values for a given network and selecting the value with a best-fit linear relationship between  $\chi$  and elevation (Perron & Royden, 2013). In many real landscapes which are undergoing transient adjustment, however,  $k_s$  (or  $k_{sn}$ ) may vary spatially. Alternative approaches have attempted to fit a number of linear segments to  $\chi$ -elevation data to circumvent this problem (Mudd et al., 2014, 2018). Note that collinearity does not imply that the whole basin collapses to a single line in  $\chi$  space, but rather that locally in  $\chi$  space, i.e. by segments, tributaries and the main stem profile should be well approximated by the same line.

The collinearity prediction provides a second independent metric that can be used to determine the optimal reference concavity index ( $\theta_{opt}$ ) that does not assume that river profiles are linear in  $\chi$ -elevation space. Instead it assumes that a point anywhere on the channel network with the same  $\chi$  value will have the same elevation. This has been used as the basis for a number of techniques which calculate the concavity index by minimising the scatter between points on tributaries with the main stem channel (Goren et al., 2014; Hergarten et al., 2016; Mudd et al., 2018). The collinearity test would be rather restrictive, however, if it were limited to landscapes where  $k_s$  were uniform. Royden and Perron (2013) used solutions of the stream power law to show that collinearity holds even if there are time varying changes to a spatially homogeneous uplift or base level fall. That is, the segment-wise collinearity should hold for most of the stream network (and all if the slope exponent is unity) even if migrating knickpoints are present. The stream power law has many assumptions (e.g. Lague, 2014), but we can alternatively use geometric relationships to show that collinearity is indicative of the most likely concavity index without invoking stream power.

Two centuries ago, Playfair (1802) observed that tributary junctions often featured channels joining at a common elevation: waterfalls are not systematically present at tributary junctions. This must mean that the two contributing streams need to have eroded at the same rate as the river just downstream of the junction. Niemann et al. (2001) expanded on this geometric observation and derived an expression for the migration rate of a local channel steepening or knickpoint (called its celerity,  $Ce_h$  [L/T]) of:

$$Ce_h = \frac{1}{S_2 - S_1} \Delta E, \quad (6)$$

where  $S_1$  is the channel slope prior to disturbance,  $S_2$  is the channel slope after disturbance (e.g., due to a change in incision rate  $E$ ), and  $\Delta E$  is the difference between the incision rate before and after disturbance ( $E_1$  and  $E_2$  in units of length per time,  $\Delta E = E_2 - E_1$ ). Following Wobus et al. (2006) we can introduce drainage area into equation (6) by replacing the slope terms using equation (1).

$$Ce_h = \frac{E_2 - E_1}{k_{s2} - k_{s1}} A^\theta. \quad (7)$$

Once  $Ce_h$  is known, we can calculate the vertical celerity ( $Ce_v$ ) which is simply the horizontal celerity multiplied by the local slope after disturbance  $S_2$  (Wobus et al., 2006). The vertical celerity of a disturbance to the channel network is independent of drainage area:

$$Ce_v = \frac{E_2 - E_1}{k_{s2} - k_{s1}} k_{s2}. \quad (8)$$

Equation (8) implies that, under conditions of spatially homogeneous uplift and constant erodibility (i.e., channels with the same slope and drainage area erode at the same rate), then changes in slope will propagate vertically in elevation at a constant rate. If we begin with a landscape with constant  $k_s$  as described in equation 5 that has a collinear channel network, and propagate changes in slope at a constant vertical celerity, the network will remain collinear even if  $k_s$  becomes spatially heterogeneous.

### 2.3 Can we know if a concavity index is “correct”?

The calculations of concavity index presented above are based on models of detachment-limited incision. A number of authors have also attempted to derive the concavity index from transport-limited models (e.g., Whipple & Tucker, 2002; Tucker & Whipple, 2002; Wickert & Schildgen, 2019). Although these models are a promising approach for understanding the fluvial concavity index, it is currently challenging to test these predictions by quantifying the correct concavity index from field observations.

An alternative approach is to create simulated topography using a model that bears some resemblance to measured incision processes, impose a concavity index upon this model, and then test if the topographic methods are able to correctly extract the imposed concavity index (e.g. Mudd et al., 2018). In spatially homogeneous, steady state landscapes, both methods could extract the correct concavity index, which is unsurprising since this situation just produces a topographic surface exactly obeying equation 1. If the modelled landscapes were perturbed by changing uplift rates, or variations in erodibility, then Mudd et al. (2018) found that the slope–area method could not reliably be used to identify the imposed concavity index, we direct the interested reader to that manuscript for more details. In contrast, Mudd et al. (2018) found the collinearity approach could identify the imposed concavity index under spatial and temporal heterogeneity that might be found in a natural landscape. In particular, Mudd et al. (2018) found the segment-wise collinearity approach for determining  $\theta_{opt}$  is resilient to spatial heterogeneity in the channel steepness index introduced by time-varying uplift or base level fall, and can extract the correct  $\theta_{opt}$  value in landscapes containing migrating knickpoints and knick-zones. Therefore, for the rest of this paper, we primarily focus on extracting the concavity index using the collinearity method.

## 3 Impact of varying concavity on the channel steepness index

The channel steepness index in equation 1 ( $k_s$ ) depends on the concavity index, meaning that  $\theta$  must be set to a reference value ( $\theta_{ref}$ ) to compare  $k_s$  values across multiple basins (Wobus et al., 2006). This results in “normalized” values of the steepness index,  $k_{sn}$ . Values of the normalized steepness index,  $k_{sn}$ , have been widely correlated with either uplift rates, inferred from a range of indicators such as dated terraces (e.g., Snyder, 2000), or erosion rates, usually inferred from the concentrations of in-situ cosmogenic nuclides such as  $^{10}\text{Be}$  (e.g., Lal, 1991). In many such studies, there is a clear positive correlation between  $k_{sn}$  and inferred erosion and uplift rates (e.g., Kirby & Whip-

ple, 2001; Safran et al., 2005; DiBiase et al., 2010; Cyr et al., 2010; Scherler et al., 2014; Ouimet et al., 2009; Mandal et al., 2015; Harel et al., 2016). Broadly speaking, these results indicate that steeper channels do reflect faster erosion rates, if one controls for other factors such as lithology (e.g. Forte et al., 2016; Peifer et al., 2021) or climate (e.g. Adams et al., 2020).

If we believe that the normalized steepness index can serve as a proxy for erosion rates, and that erosion rates are correlated with uplift rates, then it follows that the normalized steepness index may be a powerful tool for detecting spatial variations in tectonic activity (e.g., Kirby & Whipple, 2012; Whittaker, 2012). However,  $k_{sn}$  is a function of the reference concavity index chosen for a given study area. If we choose the incorrect value of this  $\theta_{ref}$ , what is the potential for misinterpreting the spatial distribution of the normalized steepness index, and therefore uplift patterns?

Figure 3 depicts scenarios where changing the value of  $\theta_{ref}$  will result in substantially different interpretations of the spatial variation in  $k_{sn}$ . Figure 3a illustrates a catchment with spatial heterogeneity in  $\theta$ . If one  $\theta_{ref}$  is used for the entire catchment this can lead to dramatic differences in the calculated  $k_{sn}$  values. This behavior is also expected in  $\chi$  space, as shown in Figure 3b, where the steep slope patches, which are interpreted as representing faster erosion, appear in different locations depending on the value of  $\theta_{ref}$ . Panels **c.** and **d.** also highlight how, depending on the choice of  $\theta_{ref}$ , one might find two clearly separated values of  $k_{sn}$  within the channel network or a range of values (see inset in panel **c.**).

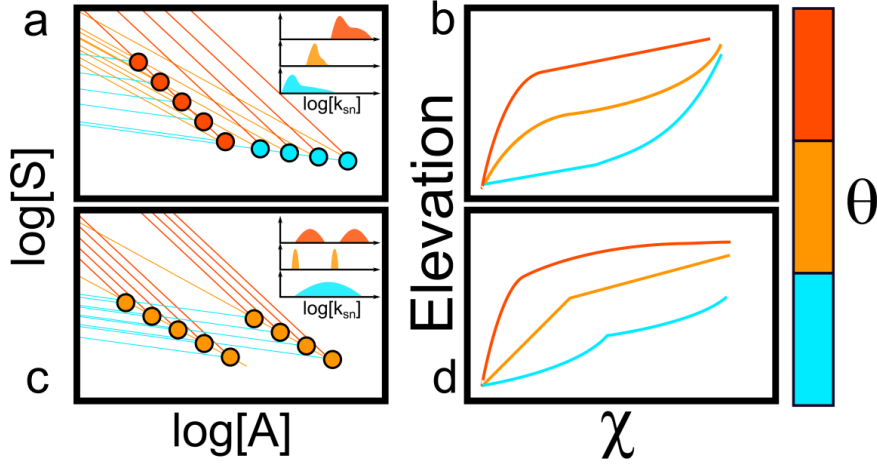


**Figure 3.** Schematic diagram exploring ways in which changing the values of the concavity index lead to differing interpretations of tectonics or erosion based on channel steepness index. Blue, orange and red colors represent low, medium and high concavities, respectively. The left column depicts  $S$ – $A$  data for two idealized catchments and the right column shows the corresponding  $\chi$ –elevation plots. The value of  $k_{sn}$  for each point in these basins will be determined by the point at which the lines intersect with the vertical axis at  $\log[A] = 0$ . Catchment 1 (top row) represents a catchment with spatial variation in concavity from a low-concavity outlet to high-concavity headwaters. Selecting one index for the entire catchment will alter the distribution of  $k_{sn}$  values as shown in the inset plots. Catchment 2 (bottom row) represents a catchment with one concavity but spatial variation in  $k_s$ . This spatial variation in  $k_s$  will only be detected if the correct concavity value is chosen.

Conceptual diagrams such as Figure 3 highlight the uncertainties in  $k_{sn}$  that are generated by uncertainties in the best fit value of  $\theta_{ref}$ . However, it is not straightforward to predict where these distortions will be greatest. One issue is that the relationship between  $k_{sn}$  and  $\theta_{ref}$  is non-linear: the order of magnitude of values of  $k_s$  (or  $k_{sn}$ ) for different values of  $\theta$  (or  $\theta_{ref}$ ) are not directly comparable. In addition, the noise of  $S$  data and sparsity of  $A$  data, caused by jumps in  $A$  at junctions, require the use of data-loss methods such as binning (e.g. Wobus et al., 2006). This disconnects single points in a channel from  $S$ – $A$  data and therefore hinders our ability to check binned values against field knowledge. Although the  $\chi$  transformation offers a means to circumvent some of these issues (Perron & Royden, 2013), it is calculated with a fixed  $\theta_{ref}$  value, meaning that landscape-scale  $\chi$  transformations may be distorted by the choice of  $\theta_{ref}$  (Figures 3b and d). Our study is focused on assessing the extent of this distortion and proposing metrics to estimate which  $\theta_{ref}$  value will least distort values of  $k_{sn}$ .

## 4 Methods

### 4.1 Quantifying concavity using disorder

We begin by looking at the uncertainty of best-fit  $\theta_{ref}$  ( $\theta_{opt}$ ) values for a single basin. We use the disorder metric, first suggested by Goren et al. (2014), that is a measure of how far tributaries depart from the main stem river and amongst themselves in  $\chi$ –elevation space (e.g. Goren et al., 2014; Hergarten et al., 2016; Mudd et al., 2018; Shelef et al., 2018). Our implementation follows the method of Hergarten et al. (2016). It ranks every point in the channel network by increasing elevation, and then checks to see if the associated  $\chi$  coordinates are similarly ranked (or not):

$$R = \sum_{i=1}^N |\chi_{s,i+1} - \chi_{s,i}|, \quad (9)$$

where the the subscript  $s, i$  represents the  $i^{th}$   $\chi$  coordinate that has been sorted by its elevation ( $\chi_{s,i}$ ). This sum,  $R$ , is minimal if elevation and  $\chi$  are related monotonically. However it scales with the absolute values of  $\chi$ , which are sensitive to the concavity index (see equation 4), so following Hergarten et al. (2016) we scale the disorder metric,  $D$ , by the maximum value of  $\chi$  in the tributary network ( $\chi_{max}$ ):

$$D(\theta) = \frac{1}{\chi_{max}(\theta)} \left( \sum_{i=1}^N |\chi_{s,i+1}(\theta) - \chi_{s,i}(\theta)| - \chi_{max}(\theta) \right). \quad (10)$$

The most likely concavity index is that which results in the lowest value of  $D(\theta)$  for the river network: a perfectly collinear population of points would have  $D(\theta) = 0$  (Hergarten et al., 2016). Although the method is based on  $\chi$  and therefore potentially sensitive to how the river network is determined (e.g. by setting a critical drainage area), sensitivity analysis in Mudd et al. (2018) demonstrated minimal sensitivity of the most likely concavity index to critical area as long as the extraction included multiple tributaries to the main stem (as the method relies on comparison between main stem and tributary channels). To constrain uncertainty, Mudd et al. (2018) created subset networks formed from the trunk stream and every possible combination of three tributaries (Figure 4). The minimum  $D(\theta)$  value was calculated for all of these combinations by iterating over potential  $\theta_{ref}$  values, creating a population of best fit concavity index values from all the combinations. The median and interquartile range were then reported.

Several authors have shown this method is effective in identifying the most likely concavity index for a watershed (Hergarten et al., 2016; Mudd et al., 2018). For a comparison of different methods utilised to constrain most-likely  $\theta_{ref}$ , we refer the interested



reader to Mudd et al. (2018). However, as explained in section 3, one may be compelled to use a different value of  $\theta_{ref}$  for a particular watershed, for example if one is comparing values of normalized channel steepness index and needs to apply a constant  $\theta_{ref}$  value across the landscape to generate  $k_{sn}$  data. We would like to know how well this fixed value of  $\theta_{ref}$  performs for multiple basins. We have therefore adapted the disorder approach to quantify sensitivity to changing  $\theta_{ref}$ . For every combination of tributaries, we calculate a value of  $D(\theta)$  for a range of  $\theta_{ref}$  values. We then normalise each value of  $D(\theta)$  by the maximum disorder value ( $D_{max}(\theta)$ ) from that range:

$$D^*(\theta) = \frac{D(\theta)}{D_{max}(\theta)} \quad (11)$$

This results in a population of  $D^*(\theta)$  values for every value of  $\theta_{ref}$  tested, and these values vary between 0 and 1 (Figure 4). If the dataset is perfectly collinear, then  $D$  will equal 0 (Hergarten et al., 2016), so normalizing by  $D_{max}(\theta)$  means  $D^*(\theta)$  spans from the maximum disorder to perfectly collinear channel networks. We can then quantify the median and lower quartile of  $D^*(\theta)$  as a function of  $\theta_{ref}$ , and from these derive estimates of the most likely  $\theta_{opt}$  value as well as some indication of how well constrained this value is. If the best fit concavity index is well constrained, the  $D^*(\theta)$  values will have a sharply defined minimum, whereas a poorly defined value will have a very broad range of  $D^*(\theta)$  values as illustrated in Figure 4c. We calculate  $D^*(\theta)$  to provide metrics reflecting how well constrained a specific  $\theta_{ref}$  is for a given watershed. Note that when studying multiple watersheds, we repeat this method within each basin and compare the statistics of these results to highlight specific aspects of the spatial variations of  $\theta_{opt}$  (e.g. median of best-fits, cumulative density of uncertainties).

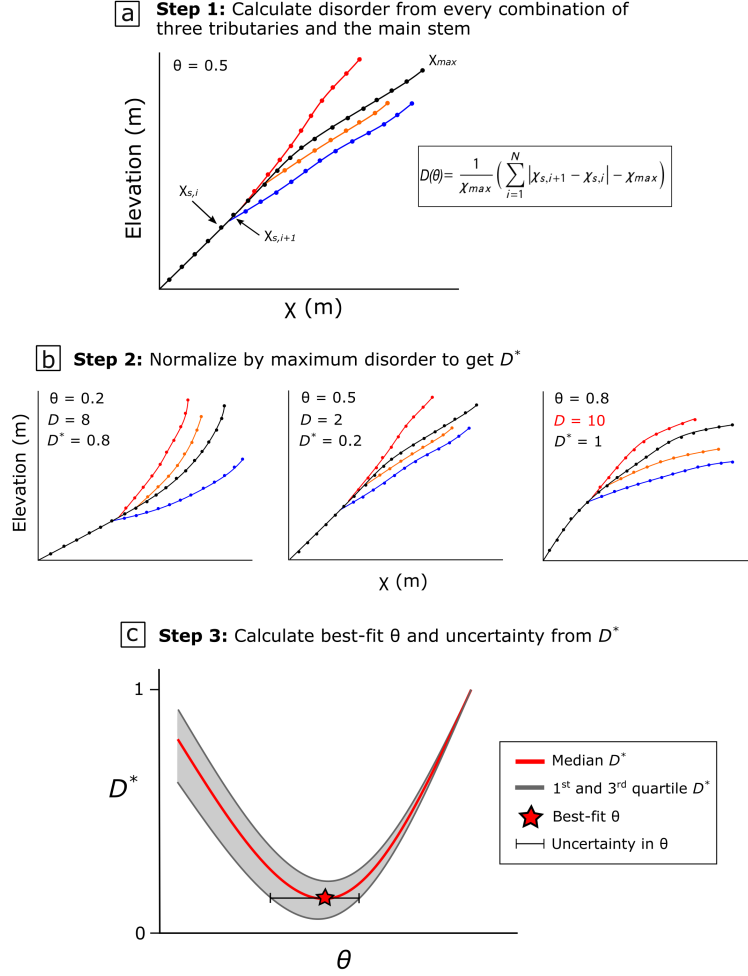


**Figure 4.** Method to determine best fit  $\theta_{opt}$  from all stream elevation data in a catchment by measuring the normalised disorder in  $\chi$  values ranked by corresponding increasing elevation within the catchment (A). Uncertainty is constrained through a bootstrapping approach to measure the disorder for all possible combinations of three tributaries plus the main stem (B) to build an uncertainty range for  $D^*$  across the range of plausible  $\theta_{ref}$  values (C).

Finding the value that minimises the disorder might suggest the most likely value for a watershed. However it is also important to quantify the goodness of this value, *i.e.* if a range of values would result in similar disorder metrics, or alternatively if small changes to the value of  $\theta_{ref}$  would lead to much greater disorder. We therefore developed a further metric for quantifying the uncertainty of  $\theta$  within a watershed. The most likely value of  $\theta_{opt}$  is defined by the minimum value of median  $D^*(\theta)$  from all combinations of tributaries extracted for each value of  $\theta_{ref}$  (Figure 4c). Alongside the median we also calculate the first quartile: these values are lower than the median for each value of  $\theta_{ref}$ , so we draw a horizontal line from the minimum of the median  $D^*$  values and mark where this intersects with the first quartile  $D^*$  values at both lesser and greater values of  $\theta_{ref}$  tested (Figure 4, panel C). We then define the uncertainty range,  $R_\theta$ , as the distance between these two points ( $max_{Q1}$  and  $min_{Q1}$ ):

$$R_{\theta} = \max_{Q1} - \min_{Q1} \quad (12)$$

Lower values  $R_{\theta}$  mean that there is less uncertainty on the best-fit  $\theta_{opt}$  (Figure 5). We can further assess the goodness of fit for  $\theta_{opt}$  for entire landscapes by calculating the cumulative distribution (CDF) of  $R_{\theta}$  values across multiple basins. The shape of the cumulative distribution is a direct proxy of the cleanness of the best-fits: a steep CDF with low values would mean that the majority of basins had relatively low uncertainties on  $\theta_{opt}$  best fit, whereas a more gradually increasing CDF would indicate that the landscape exhibits a wider range of uncertainty on  $\theta_{opt}$ .

The technique outlined above allows us to calculate the best-fit  $\theta_{opt}$  value for one particular basin. However,  $D^*(\theta)$  is less useful if we wish to constrain the most likely value of  $\theta_{opt}$  across multiple watersheds. Different basins will have a different minimum value and the normalisation of  $D^*$  only takes the maximum as reference.  $D^*(\theta)$  calculated separately for each basin can be ambiguous. Adjacent basins might have a very well constrained  $\theta_{opt}$  with a  $D^*(\theta)$  close to 0, whereas a nearby basin may have a poorly constrained fit with a higher minimum  $D^*(\theta)$ . To compensate for this variability, we also calculate a disorder metric normalized by the range of disorders within a basin, which we call  $D_r^*(\theta)$ :

$$D_r^*(\theta) = \frac{D(\theta) - D_{min}(\theta)}{D_{max}(\theta) - D_{min}(\theta)} \quad (13)$$

We can calculate  $D_r^*(\theta)$  for the reference value of  $\theta$  ( $\theta_{ref}$ ) across every basin in the landscape. If the best-fit  $\theta$  for a particular basin is equal to  $\theta_{ref}$ , then  $D_r^*$  for that basin will be 0. We can therefore interrogate the distribution of  $D_r^*(\theta)$  values for the landscape to determine how well-constrained  $\theta_{ref}$  is, and therefore how reliable our estimates of the  $k_{sn}$  will be.

## 4.2 Quantifying spatial variations of $\theta$ using S-A

The disorder metric outlined in Section 4.1 relies on comparing the main stem channel with a number of tributaries. In some cases, either where basins have very few tributaries, or if concavity along a specific channel is of interest this method is not appropriate. In these cases we use slope-area plots to quantify spatial variations in  $\theta$ , as illustrated for the Danube case study (Section 5.4). We calculate the slope of the main channel using a fixed elevation drop of 5 meters. We wish to look at broad patterns in concavity so we segment the river into reaches based on their geological and/or geographical settings, *e.g.* by sedimentary basin or upland area. In each subjectively defined reach, based on their geological and geographical context, we apply an iterative Monte Carlo sampling scheme to randomly select 80% of the points within the reach and perform linear regressions to determine a population of  $\theta$  values for each reach. This iterative method is used to constrain uncertainty in the  $\theta$  values derived from this method.

## 5 Concavity across scales

We use the collinearity method outlined in Section 4.1 to investigate concavity across a wide range of different scales, ranging from individual drainage basins to entire mountain ranges. We aim to explore how variable concavity is spatially across different regions and test our ability to constrain a representative  $\theta$  that can be used as  $\theta_{opt}$  in channel steepness index or  $\chi$  calculations.

## 5.1 Individual drainage basins

As a first step, we illustrate the collinearity method with two small watersheds in different geological contexts (Figure 5). The aim of using  $D^*(\theta)$  is to not only determine the most likely value of  $\theta$  for a given watershed, but also to determine how “wrong” other values are. This is necessary because normalized steepness index values ( $k_{sn}$ ) are frequently calculated based on an assumed reference concavity  $\theta_{ref}$ , which inevitably results in values of the channel steepness index being calculated using values of  $\theta_{ref}$  which are inappropriate for an individual basin.

The first example site (Figure 5a,b,c) is in the Loess Plateau (China). It features a relatively homogeneous substrate and relatively homogeneous concavity indices estimated from previous studies (e.g. Mudd et al., 2018; Zhang et al., 2020). The density map in Figure 5a shows  $D^*$  values for each value of  $\theta_{ref}$  tested, and for each combination of tributaries tested in the watershed. Higher densities (e.g., bright colours) mean that many of the tributary combinations returned that value of  $D^*$ . Median values minimising  $D^*$  suggest an optimal  $\theta$  ( $\theta_{opt}$  which is the most likely value of  $\theta_{ref}$ ) value of 0.425 and a  $R_\theta$  value of 0.075. A  $\chi$ -elevation plot made using this concavity (Figure 5b) shows linear channel and tributary profiles, suggesting a channel with homogeneous substrate and a constant erosion rate (Perron & Royden, 2013).

Figure 5c shows an example of two catchments which have a different  $\theta_{opt}$  from the disorder metric, highlighting the contrast in the  $\chi$ -elevation plots that can result from choosing a  $\theta_{ref}$  that is different from  $\theta_{opt}$ . Panels **b** and **e** show the  $\chi$ -elevation profile for the correct value of  $\theta_{ref}$  ( $\theta_{opt}$ ), whereas panels **c** and **f** show the impact of varying  $\theta_{ref}$  from 0.15 to 0.85. If the  $\theta_{ref}$  values in panel **c** were used to determine  $k_{sn}$ , one would predict a wide range of channel steepness indices. Low values of  $\theta_{ref}$  result in tributaries that have higher values of  $k_{sn}$  than the main stem (i.e., they are steeper in  $\chi$ -elevation space), whereas tributaries have lower values of  $k_{sn}$  than the main stem if  $\theta_{ref}$  is large. We also observe that the black dataset using  $\theta_{ref} = 0.15$  is closer to collinearity than the red dataset using  $\theta_{ref} = 0.85$  as predicted by its lower disorder value.

The second test site is a watershed located in the South-Eastern Carpathians (the outlet is 5 km NW of Buzau, Romania). The landscape is marked by spatial variations in uplift and subsidence, heterogeneous lithology (Maţenco, 2017, and references therein), and shows strong evidence of stream piracy (e.g. ter Borgh, 2013). Figure 5d presents a density plot of  $D^*$  values that feature more scatter than those of the Loess Plateau. However, the most optimal  $\theta_{opt}$ , which here is 0.275 with a  $R_\theta$  of 0.15, can still be determined from the minimum value of  $D^*(\theta)$ . Figure 5e demonstrates that the method still isolates the value of  $\theta_{ref}$  which maximises collinearity despite prominent breaks-in-slope, a small number of outlier tributaries, and many competing forcings. If we compare the  $\chi$ -elevation profiles in Figure 5f, we see that the profiles with a high value of  $\theta_{ref}$  are much more scattered than those with a low value of  $\theta_{ref}$ , which reflects the relative spread of  $D^*(\theta_{ref})$  at these  $\theta$  values depicted in the density plot in Figure 5d.

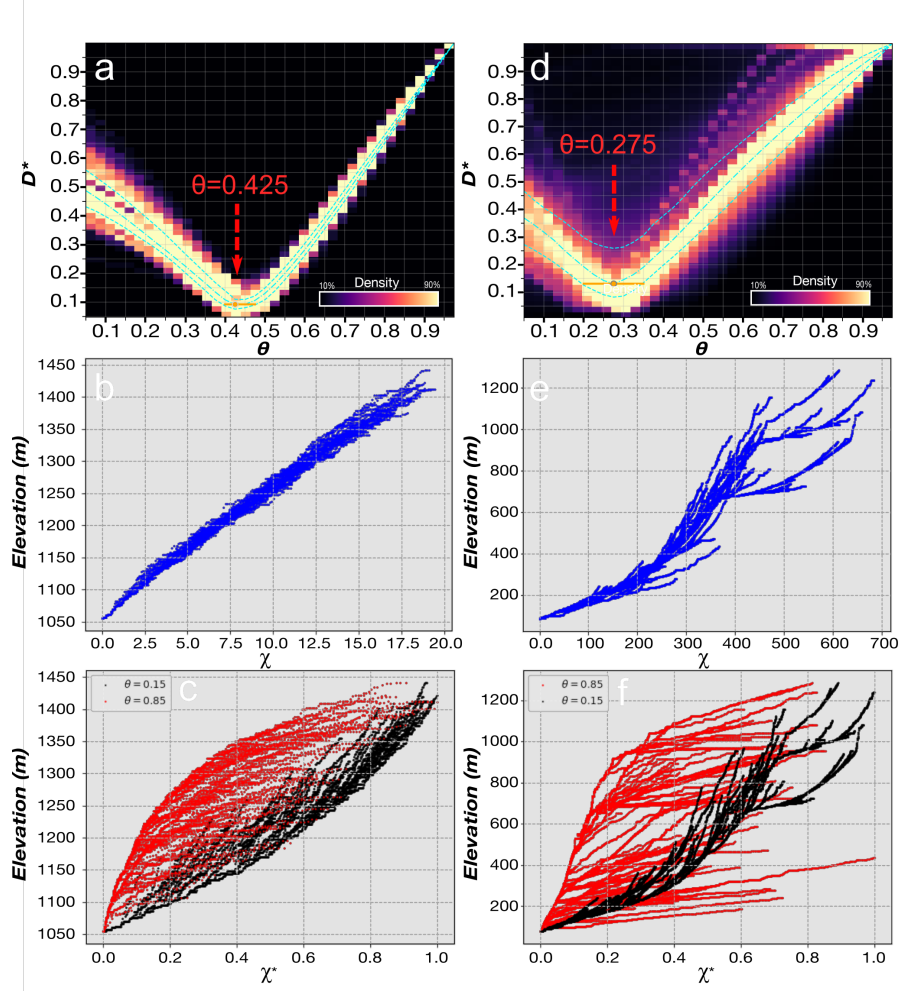


**Figure 5.**  $\theta_{opt}$  best-fit for single watershed in the Loess Plateau (a,b and c) and for the Buzau river (d,e and f) in the South-Eastern Carpathians. The watershed areas are respectively 1000  $km^2$  and 3800  $km^2$  a) and d) Density plots of the  $D^*$  for each combination of watersheds function of  $\theta_{ref}$ . It suggests  $\theta_{opt} = 0.425$  and  $R_\theta = 0.075$  with a sharp and clear minimum for the Loess Plateau and  $\theta_{opt} = 0.275$   $R_\theta = 0.15$  for Buzau. Note that the histogram is constructed combining disorder analysis of many combinations of tributaries with the main stream, see (Mudd et al., 2018) for full details about the sampling method. This can lead to minor local minima if a localised group of tributaries shows a different  $\theta_{opt}$  than the rest of the basin. b) and e)  $\chi$ -Elevation profile for the river at calculated with optimal  $\theta_{ref}$ . Note the collinearity of the profiles. c) and f) Non-dimensionalised  $\chi^* = \chi/\chi_{max}$  calculated with non-optimal  $\theta_{refs}$ . Note the high scatter compare to their optimised counterparts.

## 5.2 Distribution of $\theta$ across mountain ranges

A mountain range or discrete upland area is a convenient unit of study in geomorphology (e.g. Gilbert, 1880). To illustrate variations in the concavity index across mountain ranges, we apply our method to a range of sites showing different tectonic and lithological characteristics, as well as a range of scales: The San Gabriel Mountains (CA, USA), the Cordillera Central of Ilocos Norte (Luzon Island, Philippines), the Eastern Carpathians (Ukraine, Romania and Republic of Moldova), and the Himalayas. For each test site,

we extract all watersheds within the landscape with drainage areas from 50 km<sup>2</sup> to 1000 km<sup>2</sup>. We remove nested watersheds to avoid including the same channels multiple times. This range in drainage area provides a good balance between basins that have a number of tributaries with which to measure collinearity, and basins having a limited amount of internal heterogeneity such as faults, lithologic contacts or climate gradients.

### 5.2.1 *San Gabriel Mountains*

The San Gabriel Mountains sit within the tectonically active Transverse Ranges in Southern California (USA) (e.g. Lindvall & Rubin, 2008). DiBiase et al. (2010) quantified the erosion rates in the area using basin-wide cosmogenic radionuclides and observed positive correlations between erosion rates and  $k_{sn}$  in the region. Using linear regressions on binned  $S$ - $A$  plots, they suggested  $\theta_{ref}=0.45$  as the best-fit value. We apply our methodology to the same field area. Figure 6a shows the spatial distribution of most likely values of  $\theta_{opt}$ , *i.e* the  $\theta$  value minimising  $D^*$  for each basin, across the landscape. A frequency plot of most likely values (Figure 6b) suggests relatively low values of the concavity index with most falling between 0.25 and 0.4 (median is 0.325, and the first and fourth quartile respectively 0.275 and 0.445), which is close to the values utilised in previous studies. Figure 6c shows that more than 60% of the basins have an  $R_\theta$  below 0.2, meaning their best-fit is narrow and relatively well-defined, with some basins even showing  $R_\theta$  close to 0.

A strategy to select a representative  $\theta_{ref}$  value depends on the watersheds of interest. In our case, if we are interested in all the basins on Figure 6, we suggest selecting  $\theta_{ref} = 0.3$  to minimise distortion. This value is the  $\theta_{opt}$  for many basins, meaning that it will minimise the distortion for a high number of basins, while being very close to the median. Figure 7 can be used to assess which basins will be most disordered, that is, have the highest  $D^*$  value for a particular  $\theta_{ref}$  value. One might have less confidence in  $k_{sn}$  values extracted from basins that are highly disordered in Figure 7 when using the regional  $\theta_{ref}$  value.

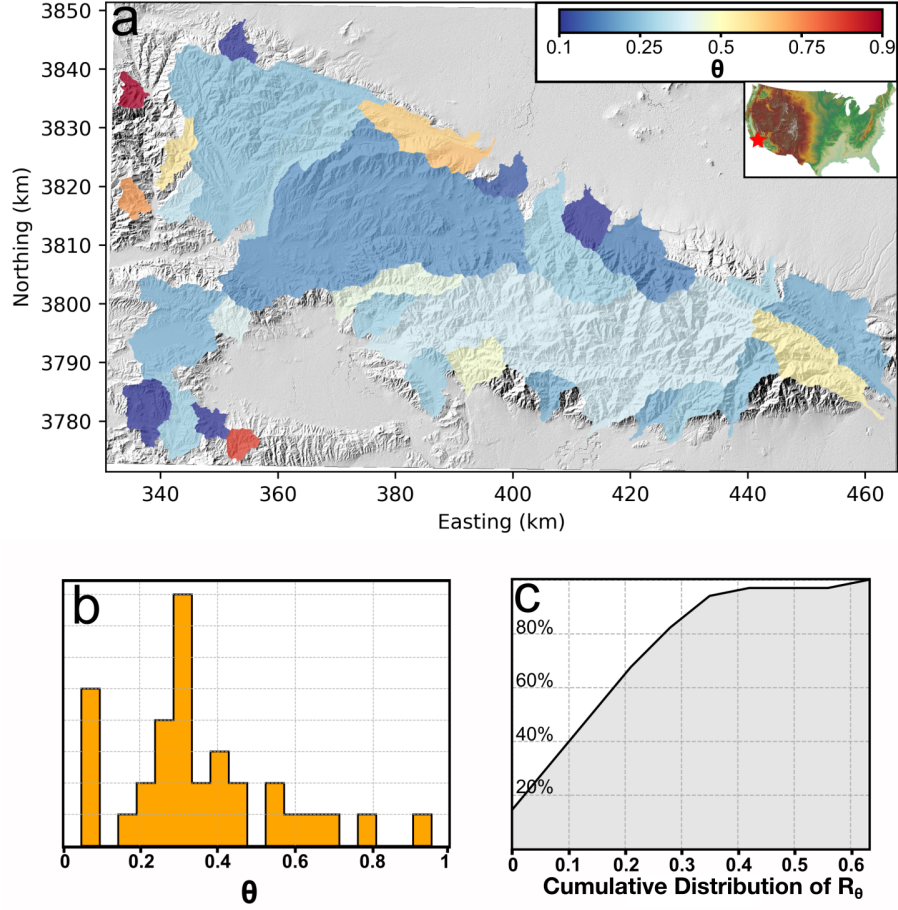


**Figure 6.** Analysis of the spatial variations in concavity index of the San Gabriel Mountains and surroundings by displaying the distribution of best-fit and their errors. The chosen base level is the topographic front, representing the switch from a mainly depositional area to a mainly incising portion of the landscape. a) Map of best fit  $\theta_{opt}$  for each catchment analysed in the area. b) Frequency distribution of the best-fit catchment values. The high concentration of  $\theta_{opt} = 0.05$  is linked to the fact that this is the minimum value considered and encompasses all best-fits lower than this. c) Cumulative distribution plot of  $R_\theta$ . This plot shows that 80% of the watersheds have  $R_\theta$  values less than 0.3.



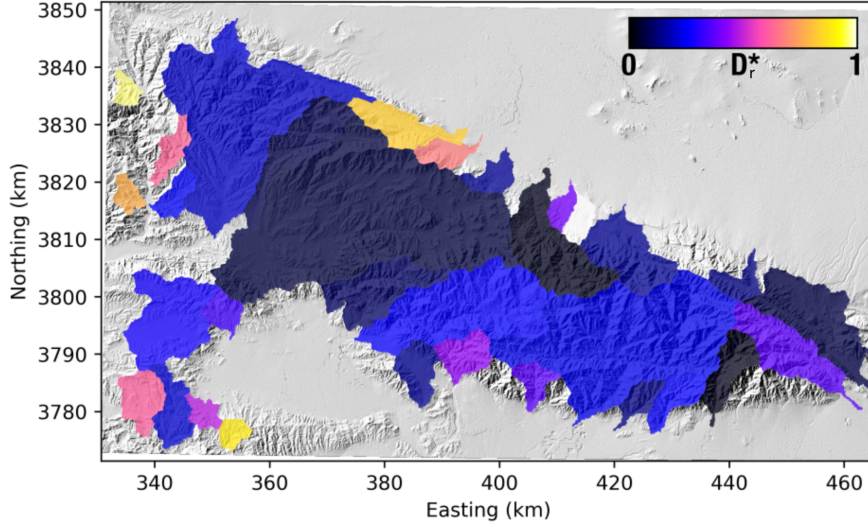


**Figure 7.**  $D_r^*$  values for each watershed for  $\theta_{ref}=0.3$ . Low values, close to 0, reflect basins that have very low disorder with this value of  $\theta_{ref}$ , whereas basins with higher  $D_r^*(\theta)$  values are much more disordered. Comparison with Figure 6 allows one to identify basins that are highly disordered because they do not share the regional best-fit  $\theta_{ref}$  (e.g., the basin in the SE corner of the study area), but it can also identify basins that have a similar best fit  $\theta_{ref}$  to the regional value, but are still somewhat disordered (e.g., the basin with an outlet on the southern side of the study area with an Easting of just over 340 km).

### 5.2.2 Cordillera Central of Ilocos Norte, Philippines

The second test site is the Cordillera Central of Ilocos Norte, in the northern part of Luzon island, Philippines. The island is bordered by doubly vergent subduction zones, one to both the east and west of the island. This tectonic forcing has led to the partition of the island by a network of active faults: the Philippine fault system features shearing, compressive, and extensional faults (e.g. Ringenbach et al., 1992; Aurelio et al., 2009). The analysis of the spatial distribution of concavity indices (Figure 8a) contrasts with the result from the San Gabriel mountains: it is much more heterogeneous. The most occurring value of  $\theta_{opt}$  for the range is 0.45 (Figure 8b), but the mountains feature basins with most likely  $\theta_{opt}$  values that vary between 0.05 and 0.95, and there is no dominant value or range of values amongst the most likely  $\theta_{opt}$  values (Figure 8b).

This heterogeneity is observable from other perspectives: Figure 8c shows the CDF of  $R_\theta$  values of the range. The curve rises much more gradually than that of Figure 6c. Only 40% of the basins have an  $R_\theta < 0.2$  and 40% of them have an  $R_\theta > 0.4$ , suggesting large uncertainties in the most likely value of  $\theta_{ref}$ .

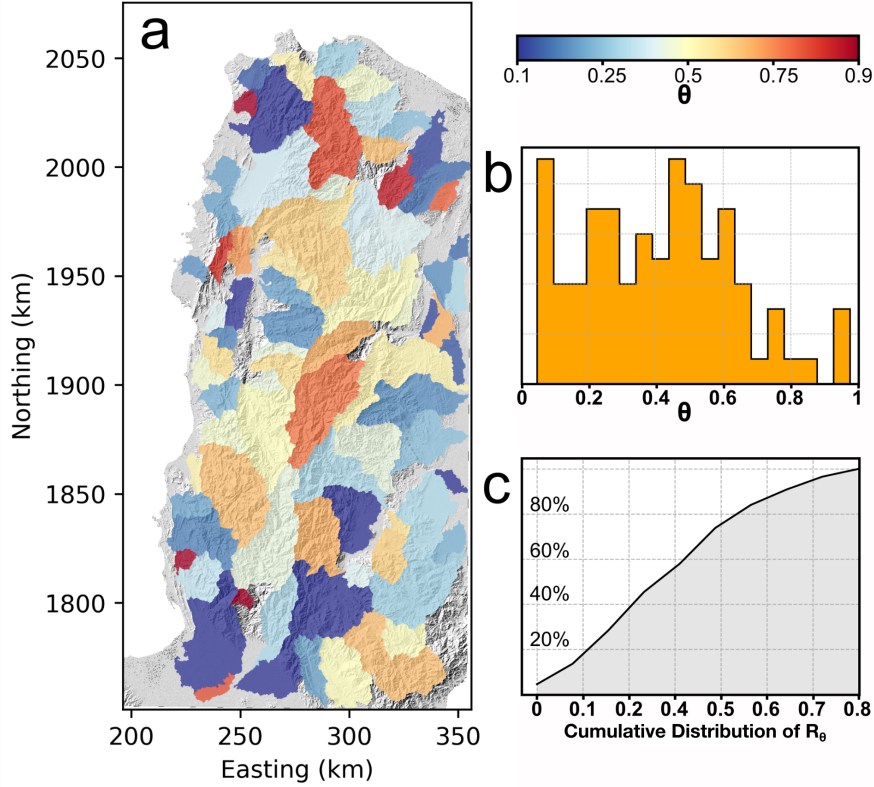


**Figure 8.** Summary of  $\theta_{opt}$  analysis for Luzon field site (Phillipines). The base level for these basins is either the sea level for the western and northern boundaries, or the switch to depositional areas for the Eastern and southern boundaries. Plots are in UTM zone 51. a) Spatial distribution of the best-fits for each watershed showing striking heterogeneity across the region. b) Distribution of  $\theta_{opt}$  values compiled for all watersheds: there is no clear peak in the best-fit  $\theta_{opt}$ . c) Cumulative density plot of the uncertainty  $R_\theta$ . The low steepness of the curve shows the spatial heterogeneity in  $\theta_{opt}$ .

### 5.2.3 The Eastern Carpathians

The Eastern Carpathians system is part of the eastern continuation of the Alpine orogeny, and is more lithologically heterogeneous than the previous two sites. In their review of the regional tectonics and its topographic expression, Mañenco (2017) (and references therein) highlighted several domains which evolved differently, ultimately controlling emergent features of the topography. The different domains are shown in Figure 9a): (i) the Southern Carpathians, composed of resistant magmatic and metamorphic rocks with the most recent significant exhumation during the Mesozoic; (ii) the Eastern Carpathians, composed of sedimentary rocks of variable strength and fewer magmato-metamorphic massifs, with exhumation history from late Miocene to present in localised sections; (iii) The Transylvanian Basin, an uplifted back-arc basin with potential drainage reorganisation (ter Borgh, 2013); (iv) The Getic and Focsani depressions, made of alluvial fans from the Southern Carpathians and subsidence of the active part of the Eastern Carpathians; and (v) the European Foreland, the foreland basin of the Eastern Carpathians and part of the European Shield (Mañenco, 2017, and references therein).

Figure 9 presents a summary of the concavity index distribution within the Eastern Carpathians. Figure 9b shows the most likely values of  $\theta_{opt}$  are widely distributed,

but the distribution is centered around 0.625, excluding a large number of values with a best fit of  $\theta_{opt} < 0.05$ . Figure 9c suggests that the different domains behave differently. The Getic and Focsani depressions primarily feature low concavities, between 0.2 and 0.4. Basins in the Southern Carpathians feature low to medium concavity with a wide range of low values between 0.1 and 0.5. The Transylvanian basin and the Eastern Carpathians present similar trends with best-fits centered on 0.5, although the relatively flat distributions suggest a less well constrained best-fit. The European Foreland, in contrast, has high  $\theta_{opt}$  values,  $> 0.6$ .

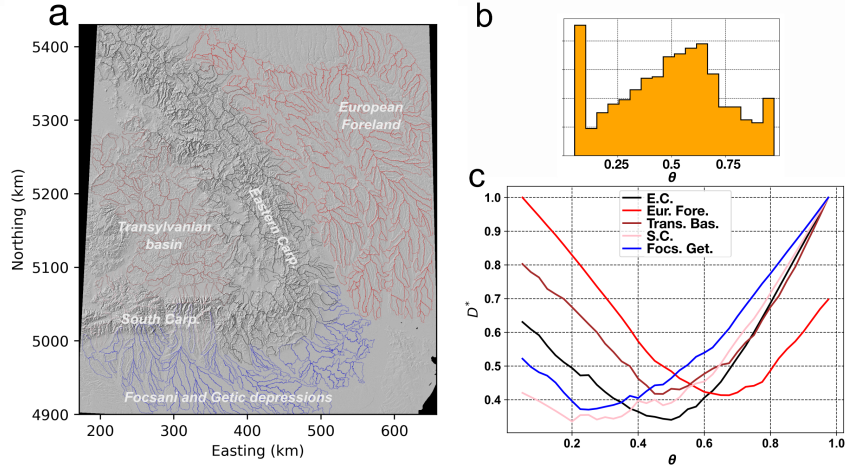


**Figure 9.** Concavity results from the Eastern Carpathians. We define a range of basin sizes for catchments (so that we can extract multiple catchments with similar drainage area) and the outlets are selected algorithmically as all catchments that fall within this range. The basins are subsequently classified based on their location. a) Watershed between  $5e^7$  and  $1e^9$  extracted colored by domain corresponding to the legend on c. The base map and subsequent units are in WGS84 UTM35N. b) Best-fit concavity across the field site. Note the peak of low values representing values lesser or equal to 0.05. c) Median profiles of the median  $D^*$  for each of the watershed by zones. Global trend can be isolated with significantly different minimums for the different area. The colors correspond to the basin outlined in a) and described in the legend.

#### 5.2.4 The Himalayan system

We also illustrate the spatial distribution of concavity in the central Himalayan system. We include in this analysis the main basins draining the range, outlined in black in Figure 10a, and their surrounding smaller basins on the Tibetan plateau and the Gangetic plain.

Himalayan River networks have been widely studied (e.g. Seeber & Gornitz, 1983; Gupta, 1997; Lavé & Avouac, 2001; Clark et al., 2004), due to the heterogeneous nature of the range's lithology and tectonics (e.g., Yin, 2006), as well as strong gradients in precipitation and discharge (Bookhagen & Burbank, 2010) and the influence of glacial processes on catchment morphology. We find strong variations in  $\theta$  values (Figure 10). Within the mountain belt, the most likely  $\theta_{opt}$  values are centred around 0.45, but large numbers of basins have most likely values between 0.05 to 0.7. Subtle patterns may be recognised; for example the patch of high concavity at Easting 750 km - Northing 3250 km,

or the strip of low concavity just north of the basins outlined in black; but apart from systematically low concavity in the plains, no clear signal emerges. This lack of pattern suggests caution should be used in applying a single value of  $\theta_{ref}$  across the range when exploring the channel steepness index.

We also analysed the large scale expression of  $\theta$  within the major basins, outlined in black, that average the effect of more factors than smaller basins (Figure 10c). Most of the large basins have a  $\theta_{opt}$  in between 0.2 and 0.4 with large uncertainties. One basin features a very high concavity, at odds with Figure 10a, suggesting that large-scale expression of concavity might hide local heterogeneities.

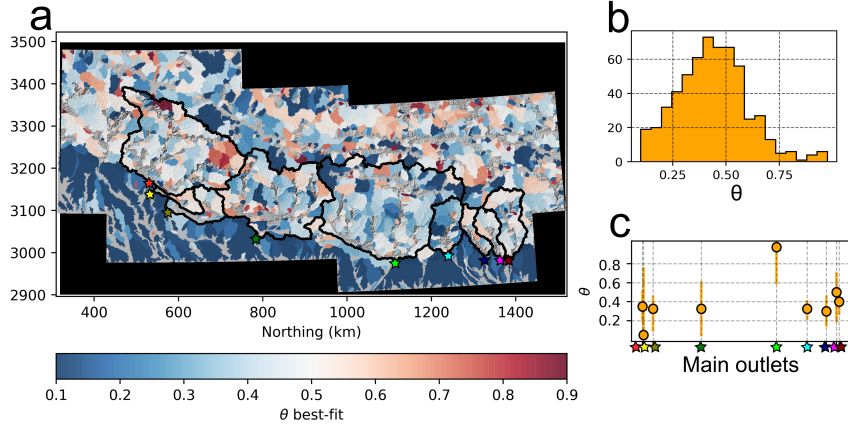


**Figure 10.** Distribution of  $\theta_{opt}$  across the Central Himalaya. a) Spatial distribution of  $\theta_{opt}$  for all watersheds in a range of drainage area from 50 to 100 km<sup>2</sup>. The black outlines are representing the main basins draining to the mountain front. The stars are their outlets and refer to figure c. b) frequency distribution of all the best fits in the study area. Note that the very low values (0.05) have been omitted here for the sake of clarity. c) Best-fit  $\theta_{opt}$  for the main drainage basins draining the Himalayas. The outlets are colored on a).

### 5.3 Variability in the concavity index across multiple basins

To give a broader picture of variation in the value of  $\theta_{opt}$ , we analysed  $\theta$  across many different landscapes, selected to represent a broad range of climate, lithology and tectonic activity. In each landscape we wish to find  $\theta_{opt}$  in numerous basins of similar size, so basins with between  $5e^6$  for the smallest and  $5e^8$  contributing pixels are selected algorithmically. In order to match with the limitations detailed in Section 2.2, we excluded major depositional areas and actively glaciated areas. We could not completely exclude basins affected by glaciation, so we have identified sites with potential glacial influence and have calculated  $\theta_{opt}$  statistics using basins with and without glaciation (see supplemental materials for the full details).

Our compilation comprises 5033 basins analysed for  $\theta_{opt}$  across a diverse range of landscapes. The median value across all these basins is 0.425, which is consistent with previous studies based on slope–area data (e.g. Tucker & Whipple, 2002). This central tendency, however, masks a very large degree of heterogeneity. The interquartile range of  $\theta_{opt}$  values is 0.225–0.575. Although we excluded major depositional areas, we note that our table makes no effort to isolate bedrock channels, and we may expect greater heterogeneity if the study area includes both alluvial and bedrock rivers (e.g., Whipple,

2004). We excluded sites that have extensive glaciation in their headwaters, but we did not eliminate all sites with glacial influence. Instead we conducted sensitivity analysis demonstrating that a dataset composed of site without any glaciation has a similar distribution of concavity index values as the entire dataset (see supplemental materials for the details).

The table includes metrics of the range of uncertainties across multiple landscapes. We hope this serves as a benchmark for authors to determine how “messy” their landscape is in a global context. The first and third quartiles for  $R_\theta$  across all 5033 basins is 0.175 and 0.375, respectively. Therefore, basins with an  $R_\theta$  value of 0.175 or less have a sharply defined  $\theta_{opt}$  compared to most basins, whereas basins with an  $R_\theta$  above 0.375 are particularly disordered: in these basins it is virtually impossible to constrain a “correct” or representative value of  $\theta$  based solely on topography.

#### 5.4 Variability along continental-scale rivers: the Danube

Our previous test sites aimed to show the variation of concavity across different scales of field site. However there is still a particular case that has not been investigated: continental-scale rivers. Here we do not aim to extract concavity values over sets of basins, but rather over a large river crossing a continent. Exploring  $\theta$  over a large river is particularly important for  $\chi$ , because the  $\chi$  coordinate integrates discharge data from base-level to top. Thus,  $\chi$  values at basin headwaters are sensitive to poorly fit values of  $\theta$  downstream (Forte & Whipple, 2018).

The Danube is the second longest river in Europe which flows for approximately 2,860 km, connecting the Alps to the Black Sea. It acts as a major source-to-sink component of the Alpine-Pannonian-Getic-Black-sea system and sets boundary condition for the erosion of the North-Eastern Alps (Matenco & Andriessen, 2013). It also crosses several sedimentary basins which are separated by gateways, each having a history of opening and closing through geological time (e.g. Leever et al., 2010, 2011).

We extracted the Danube river long profile using a pre-conditioned DEM from the HydroShed (Lehner et al., 2008), and segmented the profile by very general domains: i) the Danube delta and crossing of the Northern Dobruja range (Eastern Romania, in dark blue in figure 11); ii) the Dacic depression, foreland of the South Carpathians (light blue in figure 11); iii) the Iron Gates, the gateway between the Dacic depression and the Pannonian Basin (green in figure 11); iv) the Pannonian Basin (orange in figure 11) and the Alpine Danube (red on figure 11). Processing of concavity along the river suggest systematically low concavity on most of the sedimentary basins (between -0.15 and 0.15). The Iron gate area and the Alpine Danube show higher concavity around 0.3.



**Table 1.** Concavity indices across selected landscapes. At each site we analyse a number of basins and report the median, and first and third quartiles of the  $\theta_{opt}$  values amongst the basins. We also report the median and first and third quartiles for the range of uncertainty ( $R_\theta$ ) for individual basins. Maps showing exact locations of study areas and spatial distributions of  $\theta_{opt}$  and  $R_\theta$  can be found in the Supplemental Materials.

| Site Name                  | N<br>Basins | Median<br>$\theta$ | Q1<br>$\theta$ | Q3<br>$\theta$ | Median<br>$R_\theta$ | Q1<br>$R_\theta$ | Q3<br>$R_\theta$ |
|----------------------------|-------------|--------------------|----------------|----------------|----------------------|------------------|------------------|
| Chilean Andes              | 65          | 0.475              | 0.225          | 0.625          | 0.275                | 0.125            | 0.4              |
| North Arkansas             | 11          | 0.65               | 0.525          | 0.663          | 0.3                  | 0.2              | 0.412            |
| Bureya Massif              | 75          | 0.45               | 0.325          | 0.55           | 0.225                | 0.175            | 0.325            |
| Eastern Carpathians        | 876         | 0.5                | 0.325          | 0.65           | 0.275                | 0.175            | 0.375            |
| Caucasus                   | 366         | 0.362              | 0.175          | 0.5            | 0.25                 | 0.15             | 0.35             |
| Sierra Madre, Mexico       | 94          | 0.45               | 0.306          | 0.525          | 0.25                 | 0.131            | 0.375            |
| Corsica                    | 30          | 0.388              | 0.256          | 0.425          | 0.288                | 0.225            | 0.444            |
| Ethiopian Highlands        | 111         | 0.3                | 0.2            | 0.4            | 0.175                | 0.125            | 0.275            |
| Jebal Barez, Iran          | 54          | 0.2                | 0.106          | 0.275          | 0.175                | 0.125            | 0.25             |
| Lesotho                    | 78          | 0.475              | 0.35           | 0.569          | 0.175                | 0.1              | 0.275            |
| Luzon                      | 88          | 0.425              | 0.225          | 0.575          | 0.338                | 0.225            | 0.475            |
| Edge of Mongolian Plateau  | 107         | 0.45               | 0.35           | 0.525          | 0.225                | 0.125            | 0.338            |
| Basins along Nujang River  | 71          | 0.45               | 0.325          | 0.625          | 0.275                | 0.175            | 0.425            |
| Oregon Coast Ranges        | 26          | 0.538              | 0.338          | 0.75           | 0.25                 | 0.175            | 0.3              |
| San Gabriel Mountains      | 34          | 0.325              | 0.275          | 0.444          | 0.212                | 0.125            | 0.3              |
| Southern Altai Mountains   | 551         | 0.35               | 0.175          | 0.525          | 0.25                 | 0.15             | 0.4              |
| Southern Brazil            | 102         | 0.475              | 0.4            | 0.55           | 0.225                | 0.15             | 0.275            |
| Western South Africa       | 634         | 0.25               | 0.125          | 0.425          | 0.225                | 0.15             | 0.35             |
| Southern Wisconsin         | 60          | 0.562              | 0.45           | 0.625          | 0.2                  | 0.144            | 0.325            |
| Yemen                      | 52          | 0.4                | 0.275          | 0.506          | 0.175                | 0.125            | 0.256            |
| Atlas Mountains            | 26          | 0.4                | 0.275          | 0.5            | 0.225                | 0.175            | 0.325            |
| Dolomites                  | 28          | 0.538              | 0.35           | 0.756          | 0.338                | 0.225            | 0.5              |
| Hida Mountains             | 51          | 0.5                | 0.3            | 0.575          | 0.3                  | 0.225            | 0.438            |
| Himalayas                  | 645         | 0.4                | 0.25           | 0.525          | 0.275                | 0.175            | 0.4              |
| Allegheny Plateau          | 118         | 0.7                | 0.556          | 0.819          | 0.25                 | 0.175            | 0.394            |
| Northern Appalachians, USA | 177         | 0.525              | 0.4            | 0.675          | 0.35                 | 0.225            | 0.45             |
| Southern Appalachians, USA | 277         | 0.5                | 0.3            | 0.625          | 0.35                 | 0.225            | 0.45             |
| Olympic Mountains          | 33          | 0.575              | 0.4            | 0.675          | 0.325                | 0.2              | 0.425            |
| Pyrenees                   | 61          | 0.475              | 0.3            | 0.575          | 0.325                | 0.225            | 0.4              |
| Taiwan                     | 97          | 0.45               | 0.15           | 0.575          | 0.275                | 0.2              | 0.375            |
| Tien Shan                  | 40          | 0.612              | 0.5            | 0.756          | 0.325                | 0.25             | 0.481            |
| Zagros Mountains           | 49          | 0.475              | 0.3            | 0.625          | 0.25                 | 0.125            | 0.4              |

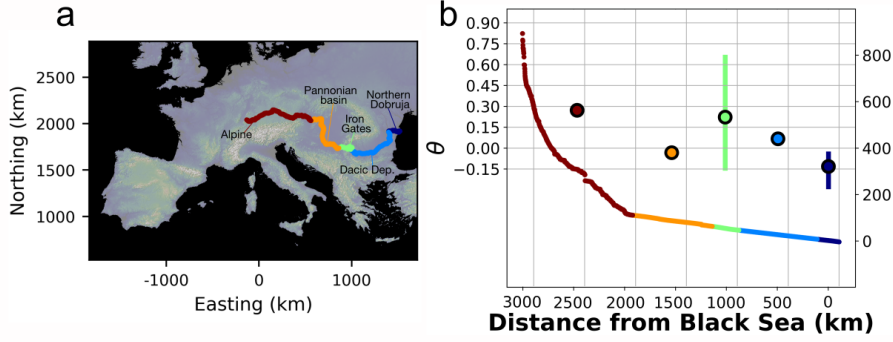


**Figure 11.** a) Map of the Danube River’s course, coloured by domains discussed in the text. Raster preconditioned by Hydroshed (Lehner et al., 2008) and projected in Lambert Conformal Conic. b) Long profile of the Danube river, with  $\theta$  for each river domain. Note the overall low concavity on  $\theta$  for most of the lowlands.

## 6 Distortion of $k_{sn}$ and $\chi$ values linked to variations in $\theta$

We have demonstrated the variability of  $\theta$  (and  $\theta_{opt}$ ) values at a wide range of scales. When studying a field site, no matter the scale of the area, one needs to assume a reference  $\theta_{ref}$  for the study in order to use  $k_{sn}$  or  $\chi$ . This forces the worker to calculate  $k_{sn}$  with  $\theta_{ref}$  values that may not be representative of some of the watersheds. Therefore, we now move on to explore how changing values of  $\theta_{ref}$  will distort  $k_{sn}$  and  $\chi$  values, and consequently our interpretation of landscape metrics. We first investigate analytical expressions of the distortion, and then illustrate the distortion using real landscapes.

### 6.1 Distortion of $k_{sn}$

Interpreting  $k_{sn}$  in a meaningful manner involves focusing on the contrasts between slope patches, *sensu* Royden and Perron (2013) across a field site. Indeed, local contrasts in  $k_{sn}$ , *i.e.* a knickpoint, are commonly interpreted as driven by phenomenon such as climatically driven base-level drop (e.g. Crosby & Whipple, 2006; Castillo et al., 2013; Prince & Spotila, 2013) or tectonically-driven changes in uplift or fault throw rates (e.g. Kirby & Whipple, 2012; Whittaker & Boulton, 2012; DeLong et al., 2017; Mitchell & Yanites, 2019; Struth et al., 2019). If contrasts between two slope patches are exaggerated, attenuated, inverted, annihilated or artificially created, spurious patterns carry a real risk for misinterpretation.

#### 6.1.1 Analytical formulation of $k_{sn}$ distortion

We consider two points in a channel network, labelled with subscripts  $M$  and  $N$ , that are characterised by their slope and drainage area ( $S_M, A_M$ ) and ( $S_N, A_N$ ). Their  $k_{sn}$  values (expressed as  $k_M$  and  $k_N$  can be expressed rearranging equation 1 as follows:

$$k_M = S_M A_M^\theta \quad (14)$$

and

$$k_N = S_N A_N^\theta \quad (15)$$



We can calculate the ratio of  $k_{sn}$  for these data points, which we call  $r_k$ , that is valid for a given  $\theta = \theta_{ref}$ :

$$r_{k,\theta} = \frac{S_M A_M^\theta}{S_N A_N^\theta} \quad (16)$$

Which we recast with a slope ratio,  $r_S$ , and an area ratio,  $r_A$ :

$$r_{k,\theta} = r_S r_A^\theta \quad (17)$$

Where  $r_S = \frac{S_M}{S_N}$  and  $r_A = \frac{A_M}{A_N}$ . To assess the distortion linked to changing the value of  $\theta$  (or  $\theta_{ref}$ ), we aim to express the ratio  $r_k$  as a function of  $\Delta\theta$ , with  $\Delta\theta$  defined as:

$$\Delta\theta = \theta_2 - \theta_1 \quad (18)$$

with  $\theta_1$  and  $\theta_2$  are the different concavities used. A logarithmic transformation can simplify comparison of  $k_{sn}$  values for different values of  $\theta_{ref}$  at sites  $M$  and  $N$ :

$$\ln[r_{k,\theta_2}] - \ln[r_{k,\theta_1}] = \ln[r_S] + \theta_2 \ln[r_A] - \ln[r_S] - \theta_1 \ln[r_A] \quad (19)$$

The slope ratios cancel because these are not affected by  $\theta$ :

$$\ln[r_{k,\theta_2}] - \ln[r_{k,\theta_1}] = \Delta\theta \ln[r_A] \quad (20)$$

We can define a factor that quantifies the distortion ratio between the two  $k_{sn}$  values as we vary  $\theta_{ref}$ , which we call the distortion factor,  $\beta_r$ :

$$\beta_r(\Delta\theta) = \frac{r_{k,\theta_2}}{r_{k,\theta_1}} = r_A^{\Delta\theta} \quad (21)$$

The distortion factor  $\beta_r(\Delta\theta)$  represents a ratio of the differences in  $k_{sn}$  at two fixed points in the channel network for two different values of concavity  $\theta$ , thus reflecting how sensitive gradients in  $k_{sn}$  are to the use of different values of concavity  $\theta_{ref}$ . Higher values of  $\beta_r$  reflect greater distortion of  $k_{sn}$ , meaning that changing  $\theta_{ref}$  values will have a greater impact on the interpretations of spatial variations in  $k_{sn}$ .

### 6.1.2 Examples of $k_{sn}$ distortion in real landscapes

We first illustrate distortion of  $k_{sn}$  with the test sites used in Figure 5. Figure 12 shows the extent of  $k_{sn}$  distortion for different hypothetical cases where local  $\theta_{opt}$  is set at a value that differs from a fixed regional value  $\theta_{ref}$ . We normalise all the  $k_{sn}$  values by their range of values, noted  $k_{sn}^*$ , to circumvent the differences in magnitude between the different values of  $\theta$ . We display their median basin-wide distribution, binned by distance from their respective outlets.

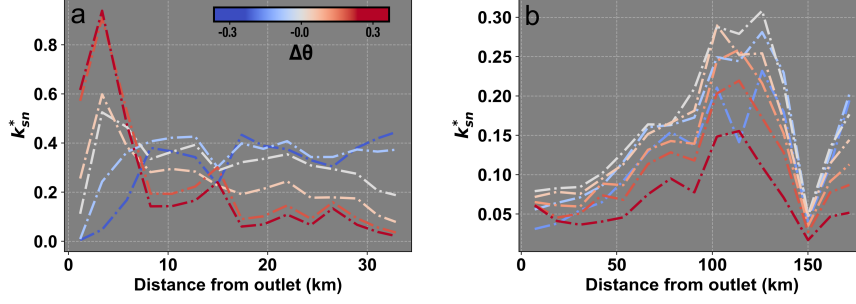


**Figure 12.** a) Distribution of  $k_{sn}^*$  – *i.e.* normalised to range – for a range of  $\theta_{opt}$  along the watershed investigated in Section 5.1a) (Loess Plateau, People’s Republic of China). The different colours correspond to  $\Delta\theta$  from a fixed value of  $\theta_{ref}=0.425$ . b) Distribution of  $k_{sn}^*$  for a range of  $\theta$  along the watershed investigated in Section 5.1d) (Buzau river, Romania). The different colours correspond to  $\Delta\theta$  from a fixed value of  $\theta_{ref}=0.275$ .

Figure 12 gives an insight of the possible distortion at the scale of a single watershed. At optimal  $\theta_{opt} = 0.425$  for the first field site (see Section 5.1), Figure 12a depicts a  $k_{sn}$  profile showing an initial increase of  $k_{sn}$  in the first 4 to 5 kilometres followed by a slight decrease in median value the rest of the profile. Using  $\theta_{ref} > \theta_{opt}$  gradually inverts this contrast by over-estimating  $k_{sn}$  in the first section of the profile. The normally decreasing part of the profile is gradually over-estimated. On the other hand, using  $\theta_{ref} < \theta_{opt}$  exaggerates the contrast between the lowest values near the outlet and the rest of the profile. The slightly decreasing pattern becomes flat or even increasing for very low  $\theta_{ref}$ .

The second and more heterogeneous field site (Buzau, Romania, see Section 5.1,  $\theta_{opt} = 0.275$ ), shows a gradual increase of  $k_{sn}$  followed by a sharp decrease near the headwaters of the network (figure 12b). Changing the value of  $\theta_{ref}$  at this site does not change the overall pattern of the channel steepness index, however overestimates of  $\theta_{ref}$  result in a flattening of the contrasts.

We also extracted illustrative  $k_{sn}$  distortion across multiple basins within the Luzon field site (Figure 13, see Section 6 for context). A number of potentially spurious patterns emerge with the use of different  $\theta_{ref}$  values to calculate  $k_{sn}$ . Here higher values of  $\theta_{ref}$  result in the largest proportion of high values of  $k_{sn}$  in the range. The zone of high  $k_{sn}$  values in Figure 13c is more extensive than the one in Figure 13a. Another systematic observation at higher  $\theta_{ref}$ , is that channels with more drainage areas feature higher values. We determined an area of interest outlined in light green in Figure 13a, b and c in order to illustrate more thoroughly some aspects of the distortion. This area includes a number of sub-basins draining to a low-relief area. At  $\theta_{ref} = 0.2$ , the larger channels have low steepness index values, and the northern section of the range has generally higher  $k_{sn}$  than the eastern section of the range. The plain has systematically low steepness indices and no sharp contrasts in  $k_{sn}$  are visible. When  $\theta_{ref} = 0.45$ ,  $k_{sn}$  values increase. Contrasts between the different sections are less pronounced but a few steeper areas do appear. At  $\theta_{ref} = 0.7$ , some of the larger rivers become steeper than the surrounding terrain. A number of sharp  $k_{sn}$  patches appear.

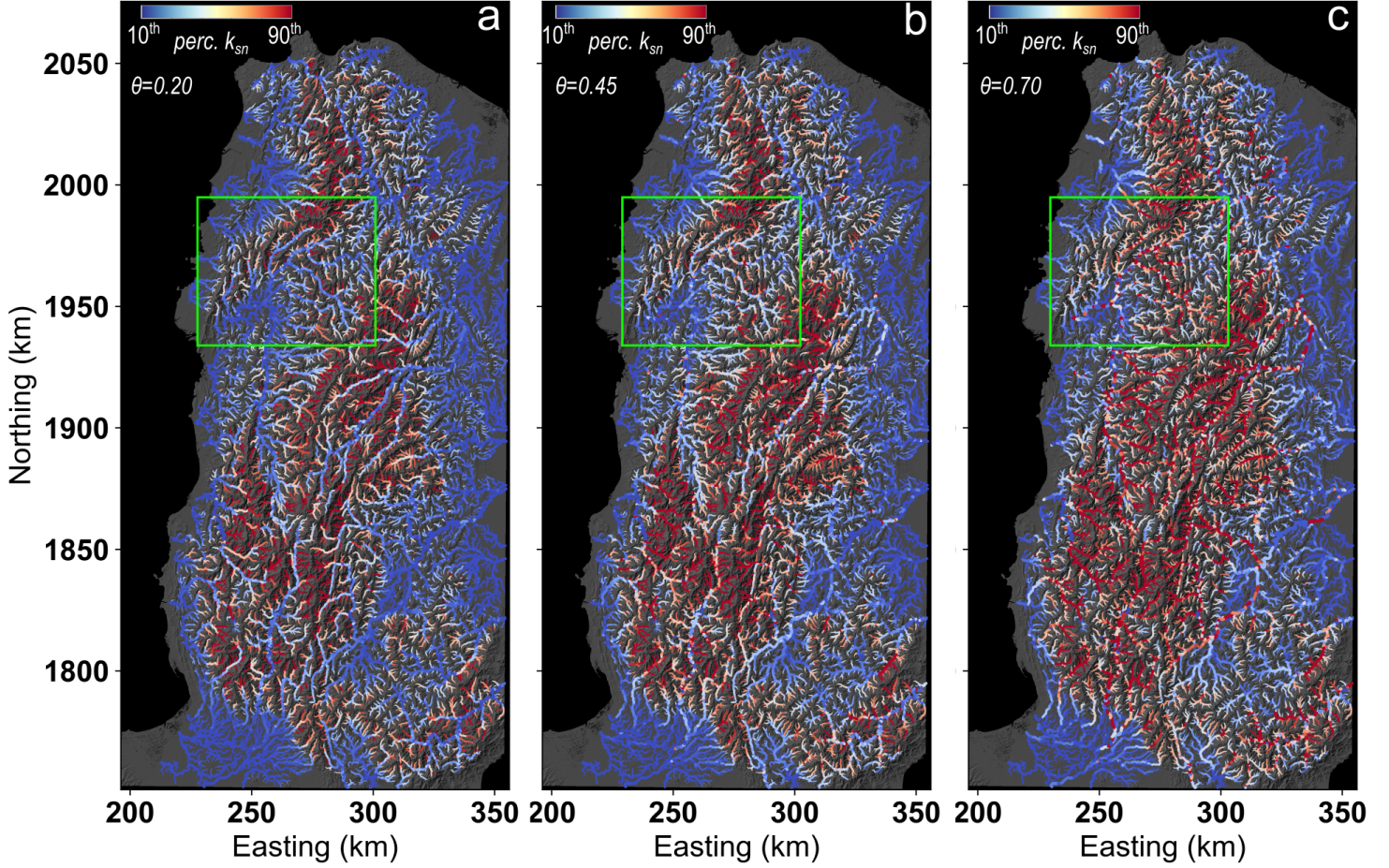


**Figure 13.** River network in the Luzon island (Philippines) coloured by  $k_{sn}$  values for different  $\theta_{ref}$ . In order to produce comparable results, the minimum and maximum colours are set to respectively the 10<sup>th</sup> and the 90<sup>th</sup> percentile of each  $k_{sn}$  populations.  $\theta_{ref}$  values have been picked in order to represent the general distribution of best-fits (see Figure 8): 0.20 for a), 0.45 for b) and 0.70 for c). River points are sized by  $\log[A]$ . Points with larger values of  $A$  are displayed where points overlap.

### 6.1.3 Subsequent implications and predictions

Equation 21 highlights a number potential biases in  $k_{sn}$  values when calculated with non-optimal  $\theta_{ref}$ . Figure 14 presents the analytical solution to the distortion  $\beta_r$ , which has the amusing property of looking like a bow tie.

Interpreting this bow tie may be slightly confusing, since  $\beta_r$  is a ratio of ratios. Let us let first give a more concrete example: consider a landscape where, at a given value of  $\theta_{ref}$  all the values of  $k_{sn}$  are the same. This means that  $r_{k,\theta_1}$  must always equal unity and that  $\beta_r$  will be equal to the ratio in channel steepness indices between two points with a drainage area threshold  $r_A$ . If the  $\theta_{ref}$  value is reduced, then channel reaches with a larger drainage area will have a smaller  $k_{sn}$  value than those with smaller drainage area. If the  $\theta_{ref}$  value is increased, then it is the reaches with larger drainage area that will increase their  $k_{sn}$  values relative to smaller channels.

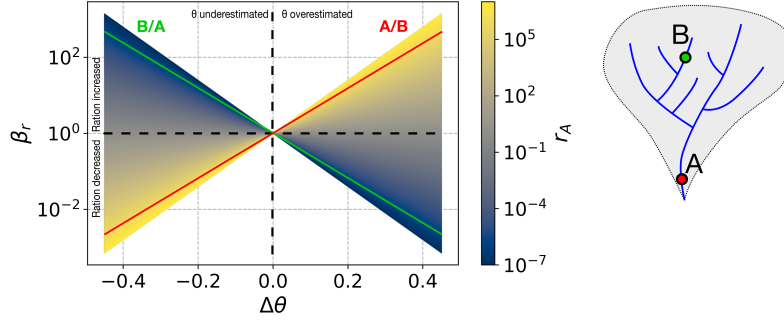


**Figure 14.** The distortion ratio ( $\beta_r$ ) as a function of the change in  $\theta_{ref}$ , colored by the ratio of drainage area between two points. Two example points of comparison are displayed for a conceptual basin, where **A** is a point with a large drainage area and **B** is a point with a low drainage. The red line reads  $\beta_r$  when comparing **A** to **B**, and the green line the inverse. For example if one overestimates  $\theta_{ref}$  by 0.3 from the local  $\theta_{opt}$ , the ratio  $^A k_{sn} / ^B k_{sn}$  will be exaggerated by a factor of nearly 100.

Having highlighted the most basic feature of Figure 14, we can expand upon the nature of distortion, which is a function of (i) how different the local  $\theta_{opt}$  is from the fixed  $\theta_{ref}$  and (ii) the differences in drainage area amongst the compared channel reaches.

To illustrate this behavior, consider two slope patches, (sensu Royden & Perron, 2013), with a contrast in  $k_{sn}$  of  $r_k$  and a contrast in drainage area  $r_A$ . Several scenarios can be considered which relate to potential distortion of  $k_{sn}$  patterns in real landscapes. First, assume that these two slope patches are contiguous, within the same river and without any significant tributary joining between them (i.e., they will have similar drainage areas). Their  $r_A$  will typically be very close to 1, *e.g.* between 0.9 and 1.1, depending on the source dataset and local context. As illustrated in Figure 14, distortion for a low ratio of drainage areas is insignificant, with a distortion of the ratio in the order of 1.05 in the worst cases. It suggests using non-optimal  $\theta_{ref}$  will not impact the importance of local knickpoints, relative to their immediate surroundings.

This might give one confidence that we do not need to worry about distortion when identifying knickpoints based on  $k_{sn}$  data. However, many studies base interpretation of factors driving the presence of knickpoints by their spatial distribution (e.g. Crosby & Whipple, 2006; Whittaker & Boulton, 2012; Mitchell & Yanites, 2019). Because river channels feature many fluctuations in gradient, simply looking for changes in  $k_{sn}$  may result in large numbers of potential knickpoints (e.g. Gailleton et al., 2019), so we must compare the relative magnitude of knickpoints in different channels, which will inevitably have different drainage areas. In this case distortion due to non-optimal  $\theta_{ref}$  becomes problematic. Consider the case where we have two knickpoints with a similar change in channel steepness across the knickpoint if  $\theta_{ref}$  is set equal to  $\theta_{opt}$ . One of these is in a small tributary (*e.g.*  $1e^5 m^2$ ) whereas the other is in a larger main stem channel (*e.g.*  $1e^9 m^2$ ,  $r_A$  in the order of  $1e4$ ). If we change  $\theta_{ref}$  away from  $\theta_{opt}$ , the distortion  $\beta_r$  can rapidly rise up to 20 times higher or lower depending on the  $\delta\theta$  (one knickpoint will appear 20 times steeper than the other). This confirms earlier observations from topographic analysis suggesting the location of contrasts in  $k_{sn}$  does not move with different values of  $\theta_{ref}$  but their relative importance would be modified (Gailleton et al., 2019).

Next, consider two slope patches of differing drainage area located within the same watershed. This can represent a wide range of possible scenarios in real landscapes, for example contiguous slope patches up and downstream of a tributary junction, slope patches



on different rivers, or slope patches on the same river that lie some distance from each other. The resulting distortion from varying the  $\theta_{ref}$  value can either generate new contrasts, erase existing ones or even invert the steepness signals (Figure 14), as observed in the Loess Plateau in Section 6.1.2. For example, a point with lower  $k_{sn}$  in the main river relative to a tributary will see the contrast between the two shrink with potential inversion of the two values if the  $\theta_{ref}$  value is increased (i.e.,  $\Delta\theta > 0$ ). On the other hand, the ratio of  $k_{sn}$  will grow exponentially larger with  $\Delta\theta < 0$ . The exact nature of the distortion is case specific when it comes to changes in drainage area and needs to be considered carefully. Figure 14 can be used, along with constraints on  $\theta_{ref}$ , to assess the risk of distortion for particular cases. Figure 14 also shows that the key parameter in determining the degree of distortion is the range of possible drainage area ratios.

An important limitation to consider is that  $k_{sn}$  and  $\theta$ -related distortion between given points can only be calculated at equal  $\theta_{ref}$ . If we consider two adjacent basins, displaying different  $\theta_{opt}$ , the original bias linked to this  $\Delta\theta_{opt}$  is not possible to quantify. Strategies to tackle such cases are discussed further in Section 7.

#### 6.1.4 Basin-averaged $k_{sn}$

The above sections address cases where the aim is to explore the spatial distribution of  $k_{sn}$  within a basin or basins. Many authors, however, explore basin-averaged  $k_{sn}$  values in order to, for example, compare this metric with basin-averaged erosion rates (e.g. Kirby & Whipple, 2012; Cyr et al., 2010; Harel et al., 2016). Does the choice of  $\theta_{ref}$  affect the results of such studies? We address this question in two ways: first at an example site and second using a simple numerical model. Our goal is to see if changing the value of  $\theta_{ref}$  will change the ranking of basin-averaged  $k_{sn}$  values amongst studied basins.

First we extracted a number of basin-averaged  $k_{sn}$  values in the Corinth rift area (Greece). The field site has been chosen for its relative tectonic and lithologic complexity (e.g. Watkins et al., 2020). We extracted basins with a drainage area greater than  $10^7 m^2$ , with a drainage area threshold for river extraction of  $1 km^2$ . Despite the complexity of the landscape and the reasonably low area threshold (i.e. higher drainage density), the results of Figure 15 suggest that most watersheds maintain their ranking of  $k_{sn}$  values across reference concavity values. That is, the basins inferred to be the steepest will remain so regardless of the choice of  $\theta_{ref}$ .

Results from the Corinth Rift suggest that for studies of basin-averaged  $k_{sn}$ , a simple sensitivity analysis should be sufficient to identify the small number of basins that do not maintain their ranking as  $\theta_{ref}$  varies. Of these basins in the Corinth Rift, the basins that change their ranking are not immediately obvious from their morphology, and the cause of “roving” basins seems highly dependent on their internal geometry and distribution of tributaries (see the previous sections about  $k_{sn}$  distortions).

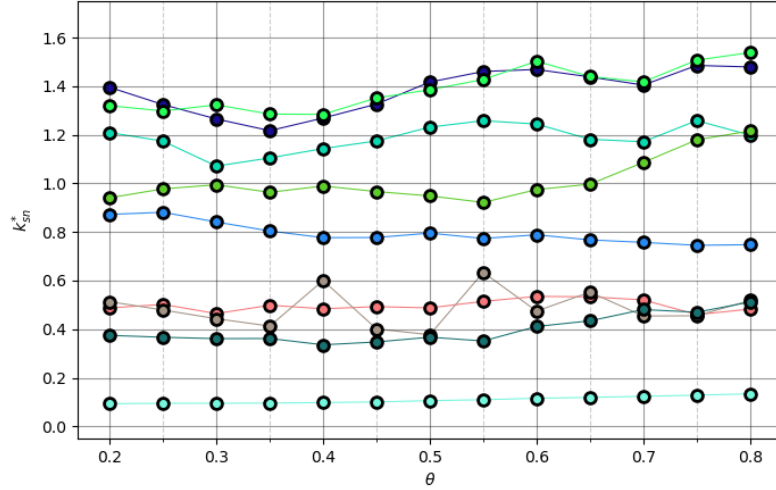


**Figure 15.** Median  $k_{sn}$  values for a number of basins in the Corinth rift area (Greece) across a range of  $\theta_{ref}$  values.  $k_{sn}^*$  is the value of basin-averaged  $k_{sn}$  normalised by its median value for a particular  $\theta_{ref}$  value, used to visualise the data on a common axis.

The second step we take is to explore how  $k_{sn}$  values reflect erosion rates across  $\theta_{ref}$  values using numerical simulations. We use the landscape evolution modelling framework fastscape (Bovy, 2021) to simulate topography through time. We use a relatively simple model configuration: we solve the stream power incision model (Howard & Kerby, 1983) using a D8 steepest descent flow routing and the implicit finite difference scheme as described in Braun and Willett (2013). The governing equation is:

$$\frac{dz}{dt} = U(x) - K(x)A(x)^m \frac{dz^n}{dx} \quad (22)$$

where  $U(x)$  is the uplift rate in [L/t],  $K(x)$  the erodibility coefficient,  $A$  the upstream drainage area and  $m$  and  $n$  the area and slope exponents, respectively. Within this framework, one can control the “real” concavity index  $\theta_{opt} = m/n$ . For this exercise, we utilise spatial variations in  $K$  to simulate landscape complexity as it has been demonstrated to represent many different factors - climatic and lithologic being the most prominent e.g. Whipple et al. (2013). Taking advantage of the modular design of fastscape’s backend (Bovy et al., 2021), we developed (Gailleton, 2021), a module to (i) simulate landscapes with 3D tilted lithologies (similar to Forte et al. (2016) or Barnhart et al. (2018)), and (ii) extract geomorphometrics from the simulated topography. Full details about the implementation can be found in the supplemental materials.

To explore the impact of  $\theta_{ref}$  on the relationship between basin-averaged  $k_{sn}$  and erosion rate, we ran 4 different model scenarios where we varied both the erodibility ( $K$ ) and the values of  $m$  and  $n$  which control the  $\theta_{opt}$  for the simulation. The results of these simulations are shown in Figure 16. We plot the results of the simulations separately to test the consistency of the relationship between  $E$  and  $k_{sn}$  within different scenarios. We note that the base relationship between  $E$  and  $k_{sn}$  in our model will be strongly affected by variations in the  $m$  and  $n$  exponents, which are held constant for each simulation. In real landscapes, these exponents may vary. For example, Gasparini and Brandon (2011) found different erosion thresholds or probability distributions of discharges in bedrock erosion rates could be replicated by changing the value of  $n$ , and empirical studies have

found a wide range of  $n$  values in varied landscapes (Harel et al., 2016), so it is not difficult to imagine a mountain range with a diversity of  $n$  values, which would strongly bias global relationship between  $E$  and  $k_{sn}$  before any potential  $\theta_{ref}$ -related effect.

The first scenario was a control run with homogeneous lithology,  $m = 0.45$  and  $n = 1$  (circle symbol). We then ran 3 scenarios with tilted rock units with varying erodibility: one with  $m = 0.9$  and  $n = 2$  ( $\theta_{opt} = 0.45$ , square symbol); one with  $m = 0.3$  and  $n = 1$  ( $\theta_{opt} = 0.3$ , up triangle symbol); and one with  $m = 0.6$  and  $n = 1$  ( $\theta_{opt} = 0.6$ , up triangle symbol). For each model run we calculated basin-averaged erosion rates as well as basin-averaged  $k_{sn}$  with three different values of  $\theta_{ref}$ : 0.3, 0.45, and 0.6. This allows us to compare the relationship between basin-averaged  $k_{sn}$  and erosion rates with different values of  $\theta_{ref}$ .

The different model runs have different imposed  $\theta_{opt}$  values yet the power law relationship between  $E$  and  $k_{sn}$  is relatively robust: the effect of variations in  $K$  for different values of  $m$  and  $n$  overprints potential distortion induced by using  $\theta_{ref} \neq \theta_{opt}$ . The implication is that a poorly fitting  $\theta_{ref}$  value or a single  $\theta_{ref}$  value for a highly heterogeneous landscape used to calculate  $k_{sn}$  values would be able to reasonably represent the distribution of  $E$  amongst basins, especially when erosion rates are high. This statement only holds, however, if all the sources of heterogeneity are constrained ( $K$ ,  $m$  and  $n$ ): a “blind” analysis with arbitrary parameters will produce biased based results.



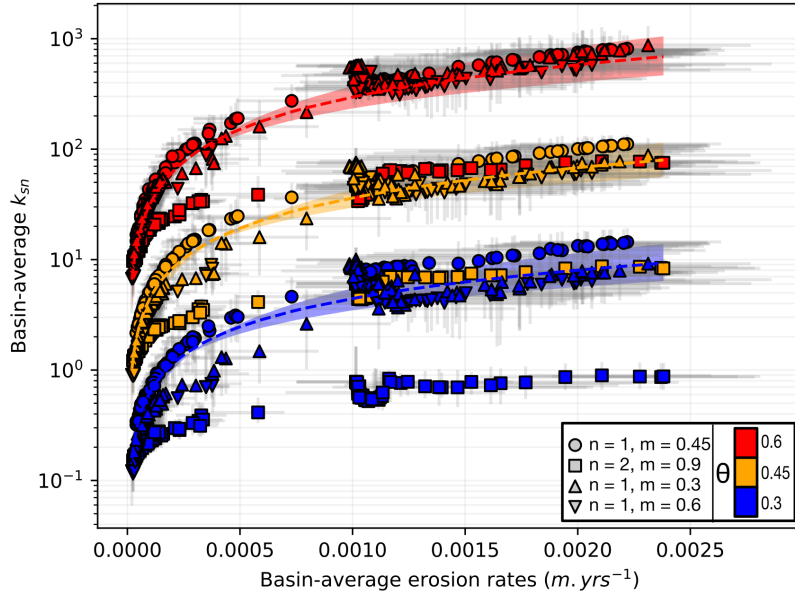


**Figure 16.** Basin averaged  $k_{sn}$  (calculated for three values of  $\theta_{ref}$ ) and erosion rates  $E$  within those basins. The data has been obtained by running four different LEM simulations with different parameters, and plotted all together in order to simulate the complexity of a natural mountain range (juxtaposed watershed with different  $\theta_{opt}$  and lithology for example). The different scenarios are: (i) homogeneous lithology,  $m = 0.45$  and  $n = 1$  (circle symbol); (ii) 3D tilted landscape with  $m = 0.9$  and  $n = 2$  (square symbol); (iii) 3D tilted landscape with  $m = 0.3$  and  $n = 1$  (up triangle symbol); and (iv) 3D tilted landscape with  $m = 0.6$  and  $n = 1$  (down triangle symbol). The  $k_{sn}$  values calculated with different  $\theta_{ref}$  values are plotted in different colours, and we plot power law curves through all  $k_{sn}$  vs  $E$  data for each value of  $\theta_{ref}$ . One can see that circles and both triangle data sets for each color fall near the power law regression of each color, particularly for rapidly eroding landscapes.

## 6.2 Influence of concavity values on the distortion of the $\chi$ coordinate

### 6.2.1 Analytical formulation of $\chi$ distortion

Expressing the analytical distortion of  $\chi$  linked to varying concavity is less straightforward than for  $k_{sn}$ , which is solely defined by constant  $S$  and  $A$  values. The  $\chi$  coordinate at a given point  $x$  of the river profile, is dependent on the downstream river network and tributaries as it integrates  $(A_0/A(x))^\theta$  from the outlet to  $x$ . This has two direct consequences.

First, the  $\chi$  value depends on the location of base level,  $x_0$ . There are several approaches to selecting a base level that may be adopted, depending on the context of the study: sea level, a fixed elevation from multiple channels, a change in geomorphic process (e.g. upland catchment transitions to a fan), or a single common point in a main stem channel. Several authors have discussed the impact of selecting the base level from amongst these choices (e.g. Forte & Whipple, 2018; Seagren & Schoenbohm, 2019), and we direct the interested reader to Figure 2 in Forte and Whipple (2018) for an illustration of the impact of base level choice on  $\chi$  contrasts.

Secondly, solving for distortion requires constraining the downstream shape of the river network. However, river flow distance  $x$  as a function of drainage area varies from river to another. For an analytical solution, we use an approximation by expressing the distance from the outlet,  $x$ , as a function of drainage area,  $A$ :

$$A(x) = (X_0 - x)^\rho \quad (23)$$

where  $X_0$  is the maximum distance of the river to the outlet (*i.e.* the distance from the source to the chosen base level), and  $\rho$  a positive exponent approximating the rate at which drainage area decreases toward the headwaters. This is a variation of Hack's law (Hack, 1957) similar to the approach of Willett (2010), as Hack's law described  $A$  as a function of flow distance downstream. Although very simplified, equation 23 can simulate realistic drainage area distribution along river profiles. We can then use the standard definition of the  $\chi$  coordinate (e.g. Perron & Royden, 2013):

$$\chi(x) = \int_{x_b}^x \left[ \frac{A_0}{(X_0 - x)^\rho} \right]^\theta dx \quad (24)$$

Integrated, this becomes

$$\chi(x) = \frac{A_0^\theta (X_0 - x)^{(1-\rho\theta)}}{\rho\theta - 1} - \frac{A_0^\theta (X_0 - x_b)^{(1-\rho\theta)}}{\rho\theta - 1} \quad (25)$$

Note that these solutions only apply when  $\rho\theta$  does not equal 1, but the above solution applies in virtually all natural examples. By definition, the outlet,  $x_b$ , has a coordinate of 0 ( $x$  is defined as the distance from the outlet), so inserting this we arrive at:

$$\chi = \frac{A_0^\theta}{\rho\theta - 1} \left[ (X_0 - x)^{(1-\rho\theta)} - X_0^{(1-\rho\theta)} \right] \quad (26)$$

Willett et al. (2014) suggested that differences in the  $\chi$  coordinate across drainage divides indicated disequilibrium in tectonic forcing and that drainage divides would migrate away from the side of the divide with a lower  $\chi$  value. Conversely, if the  $\chi$  value is the same on either side of the divide for two points with the same elevation, then the divide should be stable. The  $\chi$  coordinate used to evaluate differences across divides is typically extracted at a critical drainage area ( $A_c$ ) (e.g. Willett et al., 2014; Forte & Whipple, 2018). We note that this method of looking across the divide does not account for local relief or slope asymmetry across the divide, for which one would use the so-called Gilbert metrics (Forte & Whipple, 2018).

If we follow standard practise and measure  $\chi$  at a critical drainage area on either side of the divide, we can explore the impact of changing  $\theta_{ref}$  on distortion of the  $\chi$  coordinate. We set  $A = A_c$  and then we further simplify equation 26 by setting  $A_0 = 1 \text{ m}^2$  (this is the value chosen in most studies). We can calculate the distance from the outlet of this critical drainage area from equation 23:

$$x_c = X_0 - A_c^{1/\rho} \quad (27)$$

Inserting equation 27 into equation 26 and setting  $A_0 = 1 \text{ m}^2$ , we arrive at:

$$\chi_d = \frac{1}{\rho\theta - 1} \left( A_c^{1/\rho - \theta} - X_0^{(1-\rho\theta)} \right) \quad (28)$$

Now consider two points on either side of a divide with the same elevation and the same  $\chi$  coordinate. The basins on either side of the divide could have different topology, so they could have different values of  $\rho$  and different values of  $X_0$ . If we call these values in the second catchment  $\rho_1$  and  $X_1$ , we can fix the two  $\chi$  coordinates to the same value:

$$\frac{1}{\rho\theta - 1} \left( A_c^{1/\rho - \theta} - X_0^{(1 - \rho\theta)} \right) = \frac{1}{\rho_1\theta - 1} \left( A_c^{1/\rho_1 - \theta} - X_1^{(1 - \rho_1\theta)} \right) \quad (29)$$

Equation 29 is used to calculate, numerically, the value of  $\rho_1$  for set values of  $X_0$ ,  $\rho$ , and  $X_1$ .

Using these values of  $\rho$ ,  $X_0$ ,  $\rho_1$ , and  $X_1$  from basins that have the same value of  $\chi$  at a critical drainage area of  $A_c$ , and which we have defined as being at equilibrium so therefore having the same elevation at these points, we can then alter the value of  $\theta$  by some offset,  $\Delta\theta$ . When  $\theta$  is modified, the  $\chi$  coordinate will change in each basin as it needs to be set to a  $\theta_{ref}$  for the whole area. But the two new  $\chi$  values will not be the same, generating an difference in  $\chi$  at the divide that is an artefact of choosing an incorrect value of  $\theta$ .

We find that the offset in  $\chi$  at the divide caused by selecting an “incorrect” value of  $\theta$  is most sensitive to the correct value of  $\theta_{opt}$ , the value of  $\Delta\theta$ , and the ratio between the lengths of the basins that share a divide,  $X_1/X_0$ . We plot results as the percent offset in  $\chi$  at the divide, which under some parameter values can exceed 40% (Figure 17).

Spurious offsets in  $\chi$  at the divide are greater when the correct value of  $\theta_{ref}$  is smaller. Unsurprisingly, offsets are greater for greater values of  $\Delta\theta$ . The value of  $\chi$  is greater in the longer catchment if  $\theta_{ref}$  has been overestimated (e.g.,  $\Delta\theta < 0$ ). In the nomenclature of Willett et al. (2014), if  $\theta_{ref}$  has been overestimated, the shorter basin will spuriously appear to be the aggressor. We have shown in Section 5.3 that most likely values of  $\theta_{opt}$  can vary substantially from the central value of 0.45. If the most likely value is high, such as in the Allegheny Plateau or in the Ukraine (Table 5.3), the distortion for choosing a concavity index of 0.45 will result in relatively small distortions of around 10%, but the errors will be much larger in locations with low concavity values if a  $\theta_{ref}$  value of 0.45 is used. We should remind the reader that our analytical examples use the rudimentary approximation of the relationship between length and area described by equation 23, so we now move on to examples in real catchments.

### 6.2.2 Illustration of $\chi$ distortion in real landscapes

We select 3 sites in different geographical and geological contexts to explore the ratio of  $\chi$  values across selected divides for a range of  $\theta_{ref}$  values. Figure 18 presents the results for the three test sites. The first site (Figure 18a and d) is the island of Puerto Rico (United States of America), which is subject to differential climatic, tectonic and lithologic forcings (e.g. Pike et al., 2010). The island does feature a common base level of the Atlantic ocean as well as asymmetric river lengths on both side of the divide. The second site (Figure 18b and e) is located in the Loess Plateau (People’s Republic of China); the site described in Section 5.1 lies within this area. We fix the base level at the Wei River, close to the relief front and at similar elevation. Finally we explore the Carpathian Mountain Range (Figure 18c and f) and the main divide across the Eastern and South Eastern Carpathians, with calculation of  $\chi$  using the Black Sea as base level. For the sake of readability, we chose to display the maps with the widely used  $\theta_{ref} = 0.45$  and the  $\theta_{ref}$  tested are 0.05, 0.25, 0.45, 0.65, 0.85.

Puerto Rico’s cross-divide  $\chi$ -ratios show wide variations across  $\theta_{ref}$  values (Figure 18). Values of  $\chi$  tend to be higher on the northern side of the divide (note rotation of figure).

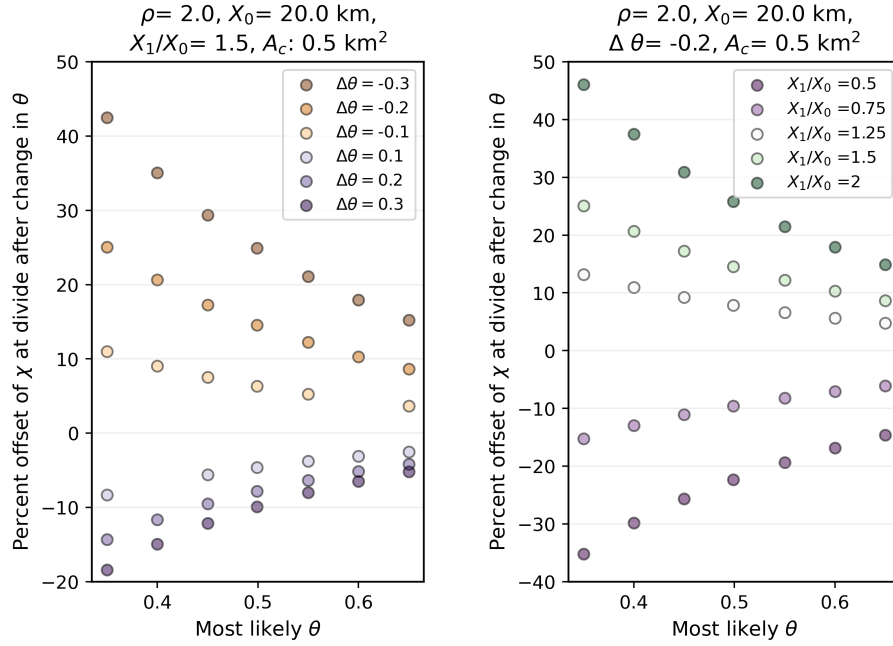


**Figure 17.** Percent difference in the  $\chi$  coordinate for two basins whose  $\chi$  values are the same for one value of  $\theta_{ref}$ , but are different lengths ( $X_0$  and  $X_1$ ), resulting in distortion of the  $\chi$  coordinate when  $\theta_{ref}$  is changed by  $\Delta\theta$ . In the left panel, we show the sensitivity to  $\Delta\theta$  whereas we show the sensitivity to the difference in length between the two catchments.

The analytical solutions (Figure 17) suggest that reducing the value of  $\theta_{ref}$  will result in longer catchments having greater values of  $\chi$  at the divide. This is illustrated in Figure 18d, where very large differences in  $\chi$  at the divide are seen for low values of  $\theta_{ref}$  at a divide distance of  $\approx 150$  km, which is where the difference in length of the northern and southern catchments is the greatest. Changing  $\chi$  values caused by changing values of  $\theta_{ref}$  can even lead to inversion of the side of the divide with greater  $\chi$ , for example at a distance of approximately 12 km along the divide, where, when  $\theta_{ref}$  is low the northern catchments have greater  $\chi$  but when  $\theta_{ref}$  is high it is the southern catchments with greater  $\chi$  values.

The Loess Plateau's cross-divide  $\chi$ -ratio at  $\theta_{ref} = 0.45$  suggests a relatively stable contrast across the area, consistent with previous findings (Willett et al., 2014). The two basins on either side of the divide have a most likely  $\theta_{ref}$  value of 0.4, very close to  $\theta_{ref} = 0.45$ . The absence of large changes in the offset of  $\chi$  across the divide for different values of  $\theta_{ref}$  in comparison to the other two study sites is also consistent with the analytical solutions: the basins on either side of the divide feature similar distances between base level and the divide. In this landscape it seems that selecting a value of  $\theta_{ref}$  inconsistent with the most likely value of  $\theta_{ref}$  would not have a large impact on the

$\chi$  offset at the divide. However if  $\chi$  is used to derive  $k_{sn}$ , the same distortion as the previous section are expected to occur.

The third test site in the Carpathians is the largest of the three and the most heterogeneous: the  $\chi$  calculation encompasses the entire whole mountain range and major sedimentary basins with very low relief as described in Section 5.4. The rivers on the southern and eastern side of the divide are linked more closely, in terms of flow distance, to the Black Sea whereas the rivers on the Western side of the divide travel around the Southern Carpathians through the Pannonian basin, flowing along the Danube and Olt rivers. As shown in the section investigating the spatial variations in  $\theta_{opt}$  in the region, the most likely values of  $\theta_{ref}$  are very heterogeneous. The patterns at the start and at the end of the divide profile are inverted when switching from low to high  $\theta_{ref}$ .

Again, we can use the analytical solutions to inform these results. At the southern section of the divide, the western basin flows along the Olt river, which we can see in Figure 18c dissecting the southern Carpathians, leading to a relatively modest difference in flow length across the divide. In the center of the divide, the basins on the western side of the divide flow a much greater distance, and so for decreasing values of  $\theta_{ref}$  the difference of  $\chi$  across the divide grows much greater, to values on the west more than 3.5 times those on the east.

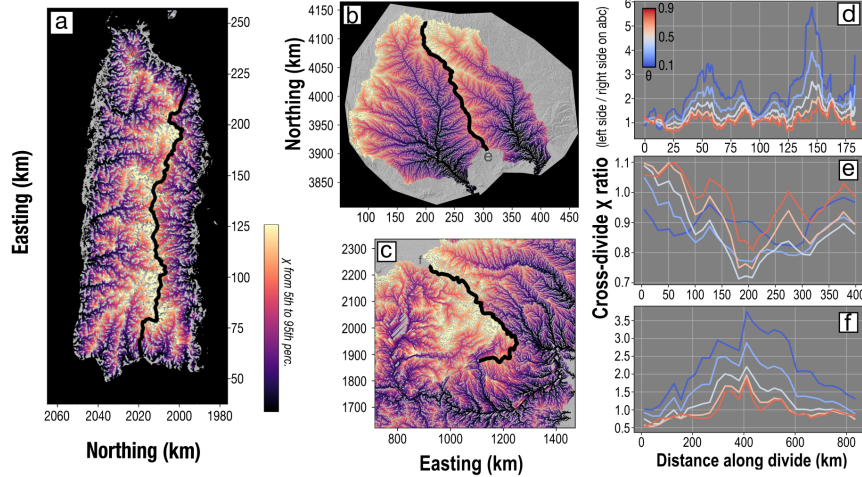


**Figure 18.** Illustration of  $\chi$  distortion effect on real landscapes. a) b) and c) show the  $\chi$  map at  $\theta_{ref} = 0.45$  for respectively Puerto Rico (WGS84-UTM19N), Loess Plateau (People’s Republic of China) and the Carpathians-Pannonian-Black Sea area (Czech Republic, Slovakia, Hungary, Romania, Bulgaria, Ukraine, Moldova, Poland, Serbia).  $\chi$  color scheme is based on the 5<sup>th</sup> to the 95<sup>th</sup> percentile for each of the respective maps. the investigated divides are displayed in bold black lines. d), e) and f) shows the cross divide for the three respective field sites. The ratio is calculated for a window of 5 km across divide for Puerto Rico and 40 km for the others.

### 6.3 $\chi$ distortion and varying erodibility

In Section 6.2.2, we demonstrated the potential magnitude of the distortion of  $\chi$  gradients across divides. We focused on the geometrical expression of the concavity index and did not assume any process-specific law in order to keep our observations general. However, we might ask how distortions in  $\chi$  caused by selecting a non-optimal value

of  $\theta_{ref}$  compare to distortions induced by spatially varied erodibility (e.g. Forte & Whipple, 2018). We use the same model including lithological complexity as used in Section 6.1.4. In these experiments, we simulate three scenarios and monitor the  $\chi$  contrast across the central divide: (i) homogeneous  $K$ , (ii) a static difference in  $K$  where the Northern half of the area is harder than the southern half and (iii) a case where we uplift a 3D block of tilted rock layers with differential  $K$ . The full details of the model parameters are reported in the supplemental materials. Results of the modelling are presented in Figure 19.

Our results suggest that the distortion of  $\chi$  ratios across drainage divides related to non-optimal  $\theta_{ref}$  cannot be disentangled from other factors but will amplify and/or reduce the signals. Results from homogeneous lithology confirm earlier observations: if both sides of the divide show homogeneous conditions of lithology, uplift, climate and planform geometry, the ratio of  $\chi$  values across the divide is very close to 1 regardless of the choice of  $\theta_{ref}$ .

When spatial variation in erodibility is introduced, however, the choice of  $\theta_{ref}$  can compound the distortion caused by heterogeneous  $K$  values (Figure 19). In the case of a different  $K$  value to the north and south of the divide, respectively  $1 \times 10^{-5}$  and  $2 \times 10^{-5}$  (the “Static  $K$ ” scenario), the difference in  $K$  values leads to a  $\chi$  ratio of approximately 1.4 once the divide has stabilised when the correct (that is model-imposed, equivalent to  $\theta_{opt}$ )  $\theta_{ref}$  value is used. For  $\theta_{ref}$  values of 0.3 or 0.6, the apparent  $\chi$  ratios become approximately 1.7 and 1.2, respectively. When we erode the landscape through tilted layers with variable  $K$ , the  $\chi$  ratio evolves through time but can drop below 0.9. However, choosing an non-optimal  $\theta_{ref}$  value can either accentuate this signal and lower the  $\chi$  ratio when  $\theta_{ref}$  values are low or switch its polarity (values greater than 1) when  $\theta_{ref}$  values are high. These simulations are by no means exhaustive, but they illustrate that distortions caused by non-optimal values of  $\theta_{ref}$  can amplify distortions caused by other factors.

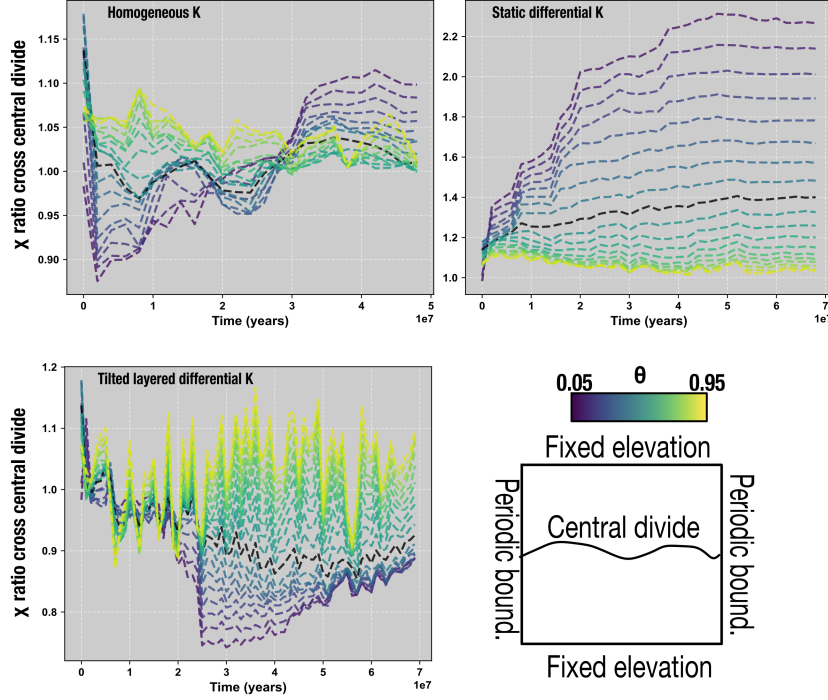


**Figure 19.** Evolution of  $\chi$  contrast across the main drainage divide through time. The thick black lines represent the results for the correct concavity  $\theta_{ref} = 0.45$  (where  $\theta_{ref} = \theta_{opt}$ ). The top-left panel displays results for homogeneous lithology. Note that contrasts are, as suspected, very close to 1 (that is, no contrast). The top-right panel shows the  $\chi$  contrast for a scenario with different values of  $K$  in the north ( $1 \times 10^{-5}$ ) and south ( $2 \times 10^{-5}$ ) halves of the model that do not change through time. As predicted by (Forte & Whipple, 2018), this scenario induces a natural  $\chi$  contrast even at equilibrium (see the black curve). The  $\chi$  contrast is reduced when  $\theta_{ref}$  is underestimated, and exaggerated if  $\theta_{ref}$  is overestimated. The bottom-left panel show the results for the tilted layered landscapes. In this scenario the signals can be amplified and the polarity of the  $\chi$  contrast can be reversed (from less than 1 to greater than one) if a non-optimal  $\theta_{ref}$  is used.

## 7 Potential implications for geomorphological studies

In this section, we discuss the potential impact of our results on studies using  $\chi$  and  $k_{sn}$  as well as potential strategies to bypass  $\theta_{ref}$ -related distortion. Because every landscape will have different ranges of  $\theta_{opt}$  among basins, it is challenging to formulate general guidelines about the potential distortion. Nevertheless, as all the distortions are functions of  $\Delta\theta$  from an optimal  $\theta_{opt}$ , constraining the range of observed best fits and their uncertainty can at least give an overview of the potential risk. Observing the sensitivity of the dataset within the range of observed  $\theta_{opt}$  values is the most straightforward test a study can make: if the contrast in  $\chi$  or different zones of  $k_{sn}$  values holds for all the values of  $\theta_{ref}$ , then  $\theta_{ref}$ -related distortion will not have a strong impact.

The  $\theta_{opt}$  dataset we calculated and analysed in this contribution has been obtained with a consistent methodology designed to explore the variations of  $\theta_{opt}$  at different scales. It is worth noting that it does not mean these  $\theta_{opt}$  are the best to use for these field sites:



any detailed study aimed at a particular site would need careful selection of basins to avoid glaciation, alluvial fans, and other features that could influence  $\theta_{opt}$ , whereas our compilation has used basins extracted algorithmically. The high degree of variation in the inter-quartile ranges and in  $R\theta$  demonstrates that local sub-basins can have different  $\theta_{opt}$  values compared to the global population. The best practice in any situation is to constrain  $\theta_{opt}$  for any field site, adapting the methodology (e.g. channel network density, selection of sub-basins depending on local constraints) function of the study aims and available data. This also applies to  $k_{sn}$ : as noted by various authors, different  $k_{sn}$  populations can be calculated from the same original data (Mudd et al., 2014; Gailleton et al., 2019; Gailleton & Mudd, 2021). Their validity only depends on the aim of the study: one may be interested in extracting local, subtle knickpoints with fine-grained segmentation of  $\chi$ -*elevation* plots, while others would extract large-scale base-level fall signals with basin-averaged data.

Regardless of whether the signal is systematic with varying  $\theta_{ref}$  or not, comparing values of  $k_{sn}$  or  $\chi$  calculated using different  $\theta_{ref}$  between basins is not possible. So, how can we compare different basins with different  $\theta_{opt}$  values while still making sure our comparison is meaningful? One potential approach is to perform some kind of normalisation: for example, in Figure 15, we normalised  $k_{sn}$  by the median value of  $k_{sn}$  in the distribution. More sophisticated approaches could be used, for example based on the modified z-score (non-parametric version of the z-score). However, these approach are limited by the fact that the normalised value can only be relative to a population. If the data density allows it, a simpler solution would be to subdivide a dataset into areas of same  $\theta_{opt}$ . This has the advantages of fully bypassing the problem, but it highly depends on the spatial variations of  $\theta_{opt}$ , which may not have the wanted spatial coverage. This is especially true for  $\chi$  contrasts at drainage divides, which needs similar  $\theta_{opt}$  on both sides of the divide to be distortion-free.

## 8 Conclusions

In this contribution, we expanded methods to determine most likely value of the reference concavity index,  $\theta_{opt}$ , using disorder metrics (e.g. Goren et al., 2014; Hergarten et al., 2016; Mudd et al., 2018; Shelef et al., 2018) that quantify both the uncertainties in  $\theta$  and the degree to which changing  $\theta$  from  $\theta_{opt}$  affect the overall disorder of the channel network. Because determination of normalized channel steepness index  $k_{sn}$  requires the assignment of a reference value of  $\theta$  ( $\theta_{ref}$ ), these metrics can give the user insight into the degree to which each basin is likely distorted by a  $\theta_{ref}$  value that differs from its most likely value ( $\theta_{opt}$ ) in a particular basin.

We go on to explore variation in most likely  $\theta_{opt}$  values across numerous catchments using the disorder metric, which can then be used as  $\theta_{ref}$ . This mirrors earlier studies which aimed to constrain  $\theta$  and  $\theta_{ref}$  using  $S$ - $A$  methods (Tucker & Whipple, 2002). Our results indicate that  $\theta_{opt}$  values have a central tendency of 0.425 similar to that suggested previously from  $S$ - $A$  analysis (e.g., Whipple et al., 2013, and references therein). The first and third quartiles across 5033 basins are 0.225 and 0.575. Given this range, we suggest authors should never assume a reference value of  $\theta_{ref}$  without testing for the most likely values.

As fixing a reference  $\theta$  will result in calculating  $k_{sn}$  using a  $\theta_{ref}$  value that is not the optimal value for each basin, we assessed, both analytically and numerically, the extent to which selection of  $\theta_{ref}$  distorts  $k_{sn}$ . When comparing values from different points in the channel network, the contrast in drainage area and  $|\Delta\theta|$  controls the magnitude of the distortion, which can reach several order of magnitudes. We demonstrate that changing  $\theta_{ref}$  can change the spatial distribution of  $k_{sn}$ , leading to the risk of misinterpretation of uplift or erosion signals. We also find that existing contrasts between areas of high and low  $k_{sn}$  can be inverted or erased. On the other hand, local adjacent contrasts with

similar drainage area are not affected, meaning that detection of knickpoints or knick-zones is unlikely to be affected by changing  $\theta_{ref}$  as long as no tributary junction is present.

We have not explored strategies to circumvent spatially varying  $\theta_{opt}$  in  $k_{sn}$  studies, but can speculate on possible approaches based on our analyses of the spatial variance of  $\theta_{opt}$  across a wide range of landscapes. One approach would be to simply constrain the range of  $\theta_{opt}$  values within the area of study and check if the spatial distribution of  $k_{sn}$  is consistent across different  $\theta_{ref}$  values. Another strategy would be to non-dimensionalize  $k_{sn}$  using, for example, a statistical representation of its distribution. Or, if one is studying a large enough landscape, a possibility is to compare populations of basins that share the same most likely value of  $\theta_{opt}$  minimising distortion. Finally, one could simply reject analysis of basins with outlying most likely  $\theta_{opt}$  values.

We also investigated how  $\chi$  values evaluated across divides are affected by changes in  $\theta_{ref}$ . Differences in the  $\chi$  coordinate have been used as a proxy for drainage divide migration (e.g. Willett et al., 2014), so if the difference in  $\chi$  across the divide is affected by changes to  $\theta_{ref}$  there is a risk of misinterpreting the presence or absence of divide migration. We first explored simple analytical solution of  $\chi$  distortion across a divide and found that basins with lower values of  $\theta_{ref}$  were more sensitive to  $\chi$  distortion. One key control is the length to base level of basins on either side of the divide. We find that for lower values of  $\theta_{ref}$ , longer basins will have increasing  $\chi$  values, so reductions in  $\theta_{ref}$  will can result in longer basins being spuriously interpreted as “victims” catchments using the nomenclature of (Willett et al., 2014). Applications on real landscapes suggested that where  $\theta_{opt}$  is spatially constant, the basins interpreted as aggressors were rarely inverted across drainage divides, but the magnitude of the  $\chi$  offset varied by, in some cases, a factor of 3 when the chosen  $\theta_{ref}$  is different than  $\theta_{opt}$ . This implies that it can be extremely challenging to robustly compare the  $\chi$  coordinate across divides in locations with spatially varying optimal  $\theta_{ref}$ .

## Acknowledgments

This project has received funding from the European Union’s EU Framework Programme for Research and Innovation Horizon 2020 under Grant Agreement No 674899 (Subitop). The digital elevation models used for this study are SRTM data (Farr et al., 2007) and have been provided by opentopography ([www.opentopography.org](http://www.opentopography.org)). This work is based on data provided by the OpenTopography Facility with support from the National Science Foundation under NSF Award Numbers 1948997, 1948994 & 1948857. The topographic analysis have been processed with lsdtopytools (Gailleton & Mudd, 2021) and the landscape evolution modelling with fastscape (Bovy, 2021) and the fastscape-litho extension (Gailleton, 2021). This research utilised Queen Mary’s Apocrita HPC facility, supported by QMUL Research-IT. <http://doi.org/10.5281/zenodo.438045>

## References

- Adams, B. A., Whipple, K. X., Forte, A. M., Heimsath, A. M., & Hodges, K. V. (2020). Climate controls on erosion in tectonically active landscapes. *Science Advances*, 6(42). Retrieved from <https://advances.sciencemag.org/content/6/42/eaaz3166> doi: 10.1126/sciadv.aaz3166
- Aurelio, M. A., Galapon, J. B., Hizon, V. T., & Sadsad, D. B. (2009, mar). Stress behavior from fault data sets within a transtensional zone, South Central Cordillera, Luzon, Philippines: Implications for mineral occurrences. *Island Arc*, 18(1), 144–154. doi: 10.1111/j.1440-1738.2009.00661.x
- Barnhart, K. R., Hutton, E., Gasparini, N. M., & Tucker, G. E. (2018). Lithology: A landlab submodule for spatially variable rock properties. *Journal of Open Source Software*, 3(30), 979. Retrieved from <https://doi.org/10.21105/joss.00979> doi: 10.21105/joss.00979

- Bookhagen, B., & Burbank, D. W. (2010). Toward a complete Himalayan hydrological budget: Spatiotemporal distribution of snowmelt and rainfall and their impact on river discharge. *Journal of Geophysical Research: Earth Surface*, 115(F3).
- Bovy, B. (2021, January). *fastscape-lem/fastscape: Release v0.1.0beta3* (Tech. Rep.). Retrieved from <https://doi.org/10.5281/zenodo.4435110> doi: 10.5281/zenodo.4435110
- Bovy, B., McBain, G. D., Gailleton, B., & Lange, R. (2021, January). *benbovy/xarray-simlab: 0.5.0* (Tech. Rep.). Retrieved from <https://doi.org/10.5281/zenodo.4469813> doi: 10.5281/zenodo.4469813
- Braun, J., & Willett, S. D. (2013). A very efficient o(n), implicit and parallel method to solve the stream power equation governing fluvial incision and landscape evolution. *Geomorphology*, 180-181, 170-179. doi: <https://doi.org/10.1016/j.geomorph.2012.10.008>
- Castillo, M., Bishop, P., & Jansen, J. D. (2013). Knickpoint retreat and transient bedrock channel morphology triggered by base-level fall in small bedrock river catchments: The case of the Isle of Jura, Scotland. *Geomorphology*, 180-181, 1-9. doi: 10.1016/j.geomorph.2012.08.023
- Chatanantavet, P., & Parker, G. (2009). Physically based modeling of bedrock incision by abrasion, plucking, and macroabrasion. *Journal of Geophysical Research: Earth Surface*, 114(F4). doi: 10.1029/2008JF001044
- Clark, M. K., Schoenbohm, L. M., Royden, L. H., Whipple, K. X., Burchfiel, B. C., Zhang, X., ... Chen, L. (2004). Surface uplift, tectonics, and erosion of eastern Tibet from large-scale drainage patterns. *Tectonics*, 23(1).
- Crosby, B. T., & Whipple, K. X. (2006). Knickpoint initiation and distribution within fluvial networks: 236 waterfalls in the Waipaoa River, North Island, New Zealand. *Geomorphology*, 82(1-2), 16-38. doi: 10.1016/j.geomorph.2005.08.023
- Cyr, A. J., Granger, D. E., Olivetti, V., & Molin, P. (2010, June). Quantifying rock uplift rates using channel steepness and cosmogenic nuclide-determined erosion rates: Examples from northern and southern Italy. *Lithosphere*, 2(3), 188-198. doi: 10.1130/L96.1
- Davis, W. M. (1899). The Geographical Cycle. *The Geographical Journal*, 14(5), 481. doi: 10.2307/1774538
- de Lapparent, A. (1896). *Leçons de géographie physique*. Paris: Masson et c', éditeurs.
- DeLong, S. B., Hilley, G. E., Prentice, C. S., Crosby, C. J., & Yokelson, I. N. (2017). Geomorphology, denudation rates, and stream channel profiles reveal patterns of mountain building adjacent to the San Andreas fault in northern California, USA. *GSA Bulletin*, 129(5), 732-749. doi: 10.1130/B31551.1
- DiBiase, R. A., & Whipple, K. X. (2011). The influence of erosion thresholds and runoff variability on the relationships among topography, climate, and erosion rate. *Journal of Geophysical Research: Earth Surface*, 116(F4). doi: 10.1029/2011JF002095
- DiBiase, R. A., Whipple, K. X., Heimsath, A. M., & Ouimet, W. B. (2010, January). Landscape form and millennial erosion rates in the San Gabriel Mountains, CA. *Earth and Planetary Science Letters*, 289(1-2), 134-144. doi: 10.1016/j.epsl.2009.10.036
- Farr, T. G., Rosen, P. A., Caro, E., Crippen, R., Duren, R., Hensley, S., ... others (2007). The shuttle radar topography mission. *Reviews of geophysics*, 45(2). doi: 10.1029/2005RG000183
- Flint, J. J. (1974). Stream gradient as a function of order, magnitude, and discharge. *Water Resources Research*, 10(5), 969-973. doi: 10.1029/WR010i005p00969
- Forte, A. M., & Whipple, K. X. (2018). Criteria and tools for determining drainage divide stability. *Earth and Planetary Science Letters*, 493, 102-117.

- Forte, A. M., Yanites, B. J., & Whipple, K. X. (2016). Complexities of landscape evolution during incision through layered stratigraphy with contrasts in rock strength. *Earth Surface Processes and Landforms*, 41(12), 1736–1757. Retrieved from <https://onlinelibrary.wiley.com/doi/abs/10.1002/esp.3947> doi: <https://doi.org/10.1002/esp.3947>
- Gailleton, B. (2021, May). *fastscape-lem/fastcape-litho: fastscape-litho 0.0.1*. Zenodo. Retrieved from <https://doi.org/10.5281/zenodo.4773791> doi: 10.5281/zenodo.4773791
- Gailleton, B., & Mudd, S. M. (2021, May). *Lsdtopotools/lsdtoppytools: lsdtoppytools*. Zenodo. Retrieved from <https://doi.org/10.5281/zenodo.4774992> doi: 10.5281/zenodo.4774992
- Gailleton, B., Mudd, S. M., Clubb, F. J., Peifer, D., & Hurst, M. D. (2019). A segmentation approach for the reproducible extraction and quantification of knickpoints from river long profiles. *Earth Surface Dynamics*, 7(1), 211–230. doi: 10.5194/esurf-7-211-2019
- Gailleton, B., Sinclair, H. D., Mudd, S. M., Graf, E. L. S., & Mañenco, L. C. (2021). Isolating Lithologic Versus Tectonic Signals of River Profiles to Test Oro-genic Models for the Eastern and Southeastern Carpathians. *Journal of Geophysical Research: Earth Surface*, 126(8), e2020JF005970. (eprint: <https://agupubs.onlinelibrary.wiley.com/doi/pdf/10.1029/2020JF005970>) doi: 10.1029/2020JF005970
- Gasparini, N. M., & Brandon, M. T. (2011). A generalized power law approximation for fluvial incision of bedrock channels. *Journal of Geophysical Research: Earth Surface*, 116(F2). doi: 10.1029/2009JF001655
- Gasparini, N. M., Bras, R. L., & Whipple, K. X. (2006). Numerical modeling of non-steady-state river profile evolution using a sediment-flux-dependent incision model. In S. D. Willett, N. Hovius, M. T. Brandon, & D. M. Fisher (Eds.), *Tectonics, Climate, and Landscape Evolution* (Vol. 398, pp. 127–141). Boulder: Geological Soc Amer Inc. doi: 10.1130/2006.2398(08)
- Gasparini, N. M., Tucker, G. E., & Bras, R. L. (2004). Network-scale dynamics of grain-size sorting: implications for downstream fining, stream-profile concavity, and drainage basin morphology. *Earth Surface Processes and Landforms*, 29(4), 401–421. doi: 10.1002/esp.1031
- Gilbert, G. K. (1880). *Report on the geology of the henry mountains*. US Government Printing Office.
- Goren, L., Fox, M., & Willett, S. D. (2014, August). Tectonics from fluvial topography using formal linear inversion: Theory and applications to the Inyo Mountains, California. *Journal of Geophysical Research: Earth Surface*, 119(8), 1651–1681. doi: 10.1002/2014JF003079
- Gupta, S. (1997, January). Himalayan drainage patterns and the origin of fluvial megafans in the Ganges foreland basin. *Geology*, 25(1), 11–14. (Publisher: GeoScienceWorld) doi: 10.1130/0091-7613(1997)025<0011:HDPATO>2.3.CO;2
- Hack, J. (1957). *Studies of longitudinal profiles in Virginia and Maryland* (U.S. Geological Survey Professional Paper No. 294-B). Washington, D.C.: United States Government Printing Office.
- Harel, M. A., Mudd, S. M., & Attal, M. (2016, September). Global analysis of the stream power law parameters based on worldwide 10be denudation rates. *Geomorphology*, 268, 184–196. doi: 10.1016/j.geomorph.2016.05.035
- Hergarten, S., Robl, J., & Stüwe, K. (2016, January). Tectonic geomorphology at small catchment sizes – extensions of the stream-power approach and the  $\chi$  method. *Earth Surface Dynamics*, 4(1), 1–9. doi: 10.5194/esurf-4-1-2016
- Howard, A. D., Dietrich, W. E., & Seidl, M. A. (1994, July). Modeling fluvial erosion on regional to continental scales. *Journal of Geophysical Research: Solid Earth*, 99(B7), 13971–13986. doi: 10.1029/94JB00744
- Howard, A. D., & Kerby, G. (1983, 06). Channel changes in badlands. *GSA Bul-*

- 1201        *letin*, 94(6), 739–752. doi: 10.1130/0016-7606(1983)94<739:CCIB>2.0.CO;2
- 1202 Kirby, E., & Whipple, K. (2001, May). Quantifying differential rock-uplift rates via
- 1203 stream profile analysis. *Geology*, 29(5), 415–418. doi: 10.1130/0091-7613(2001)
- 1204 029<0415:QDRURV>2.0.CO;2
- 1205 Kirby, E., & Whipple, K. X. (2012, November). Expression of active tectonics in ero-
- 1206 sional landscapes. *Journal of Structural Geology*, 44, 54–75. doi: 10.1016/j.jsg
- 1207 .2012.07.009
- 1208 Knopf, E. B. (1924, sep). Correlation of residual erosion surfaces in the eastern ap-
- 1209 palachian highlands. *Bulletin of the Geological Society of America*, 35(3), 633–
- 1210 668. doi: 10.1130/GSAB-35-633
- 1211 Lague, D. (2014, January). The stream power river incision model: Evidence, the-
- 1212 ory and beyond. *Earth Surface Processes and Landforms*, 39(1), 38–61. doi: 10
- 1213 .1002/esp.3462
- 1214 Lague, D., Hovius, N., & Davy, P. (2005). Discharge, discharge variability, and
- 1215 the bedrock channel profile. *Journal of Geophysical Research: Earth Surface*,
- 1216 110(F4). doi: 10.1029/2004JF000259
- 1217 Lal, D. (1991, June). Cosmic ray labeling of erosion surfaces: in situ nuclide produc-
- 1218 tion rates and erosion models. *Earth and Planetary Science Letters*, 104(2),
- 1219 424–439. doi: 10.1016/0012-821X(91)90220-C
- 1220 Lavé, J., & Avouac, J. P. (2001). Fluvial incision and tectonic uplift across the
- 1221 Himalayas of central Nepal. *Journal of Geophysical Research: Solid Earth*,
- 1222 106(B11), 26561–26591.
- 1223 Leever, K. A., Matenco, L., Garcia-Castellanos, D., & Cloetingh, S. A. (2011, apr).
- 1224 The evolution of the Danube gateway between Central and Eastern Paratethys
- 1225 (SE Europe): Insight from numerical modelling of the causes and effects of
- 1226 connectivity between basins and its expression in the sedimentary record.
- 1227 *Tectonophysics*, 502(1–2), 175–195. doi: 10.1016/j.tecto.2010.01.003
- 1228 Leever, K. A., Matenco, L., Rabagia, T., Cloetingh, S., Krijgsman, W., & Stoica, M.
- 1229 (2010, feb). Messinian sea level fall in the Dacic Basin (Eastern Paratethys):
- 1230 Palaeogeographical implications from seismic sequence stratigraphy. *Terra*
- 1231 *Nova*, 22(1), 12–17. doi: 10.1111/j.1365-3121.2009.00910.x
- 1232 Lehner, B., Verdin, K., & Jarvis, A. (2008, mar). New global hydrogra-
- 1233 phy derived from spaceborne elevation data. *Eos*, 89(10), 93–94. doi:
- 1234 10.1029/2008EO100001
- 1235 Lindvall, S. C., & Rubin, C. M. (2008). *Slip Rate Studies along the Sierra*
- 1236 *Madre–Cucamonga Fault System Using Geomorphic and Cosmogenic Surface*
- 1237 *Exposure Age Constraints: Collaborative Research with Central Washington*
- 1238 *University and William Lettis & Associates, Inc.* (Tech. Rep. No. US Geo-
- 1239 logical Survey final report 03HQGR0084). Washington, D.C.: United States
- 1240 Geological Survey.
- 1241 Mandal, S. K., Lupker, M., Burg, J.-P., Valla, P. G., Haghipour, N., & Christl, M.
- 1242 (2015, September). Spatial variability of <sup>10</sup>be-derived erosion rates across the
- 1243 southern Peninsular Indian escarpment: A key to landscape evolution across
- 1244 passive margins. *Earth and Planetary Science Letters*, 425, 154–167. doi:
- 1245 10.1016/j.epsl.2015.05.050
- 1246 Matenco, L., & Andriessen, P. (2013, April). Quantifying the mass transfer from
- 1247 mountain ranges to deposition in sedimentary basins: Source to sink studies in
- 1248 the Danube Basin-Black Sea system. *Global and Planetary Change*, 103, 1–18.
- 1249 doi: 10.1016/j.gloplacha.2013.01.003
- 1250 Mațenco, L. (2017). Tectonics and exhumation of Romanian carpathians: Infer-
- 1251 ences from kinematic and thermochronological studies. In M. Radoane &
- 1252 A. Vespremeanu-Stroe (Eds.), *Springer geography* (pp. 15–56). Cham: Springer
- 1253 International Publishing. doi: 10.1007/978-3-319-32589-7\_2
- 1254 Mitchell, N. A., & Yanites, B. J. (2019). Spatially Variable Increase in Rock Uplift
- 1255 in the Northern U.S. Cordillera Recorded in the Distribution of River Knick-



- points and Incision Depths. *Journal of Geophysical Research: Earth Surface*, 124(5), 1238–1260. doi: 10.1029/2018JF004880
- Morisawa, M. E. (1962, September). Quantitative Geomorphology of Some Watersheds in the Appalachian Plateau. *GSA Bulletin*, 73(9), 1025–1046. doi: 10.1130/0016-7606(1962)73[1025:QGOSWI]2.0.CO;2
- Mudd, S. M., Attal, M., Milodowski, D. T., Grieve, S. W., & Valters, D. A. (2014, feb). A statistical framework to quantify spatial variation in channel gradients using the integral method of channel profile analysis. *Journal of Geophysical Research: Earth Surface*, 119(2), 138–152. doi: 10.1002/2013JF002981
- Mudd, S. M., Clubb, F. J., Gailleton, B., & Hurst, M. D. (2018, jun). How concave are river channels? *Earth Surface Dynamics*, 6(2), 505–523. doi: 10.5194/esurf-6-505-2018
- Niemann, J. D., Gasparini, N. M., Tucker, G. E., & Bras, R. L. (2001, November). A quantitative evaluation of Playfair’s law and its use in testing long-term stream erosion models. *Earth Surface Processes and Landforms*, 26(12), 1317–1332. doi: 10.1002/esp.272
- Ouimet, W. B., Whipple, K. X., & Granger, D. E. (2009, July). Beyond threshold hillslopes: Channel adjustment to base-level fall in tectonically active mountain ranges. *Geology*, 37(7), 579–582. doi: 10.1130/G30013A.1
- Peifer, D., Persano, C., Hurst, M. D., Bishop, P., & Fabel, D. (2021). Growing topography due to contrasting rock types in a tectonically dead landscape. *Earth Surface Dynamics*, 9(2), 167–181. Retrieved from <https://esurf.copernicus.org/articles/9/167/2021/> doi: 10.5194/esurf-9-167-2021
- Perron, J. T., & Royden, L. H., Royden. (2013). An integral approach to bedrock river profile analysis. *Earth Surface Processes and Landforms*, 38(6), 570–576. doi: 10.1002/esp.3302
- Pike, A. S., Scatena, F. N., & Wohl, E. E. (2010). Lithological and fluvial controls on the geomorphology of tropical montane stream channels in puerto rico. *Earth Surface Processes and Landforms*, 35(12), 1402–1417. Retrieved from <https://onlinelibrary.wiley.com/doi/abs/10.1002/esp.1978> doi: <https://doi.org/10.1002/esp.1978>
- Playfair, J. (1802). *Illustrations of the Huttonian theory of the earth*. Edinburgh: Neill and Co. Printers.
- Prince, P. S., & Spotila, J. A. (2013). Evidence of transient topographic disequilibrium in a landward passive margin river system: knickpoints and paleo-landscapes of the New River basin, southern Appalachians. *Earth Surface Processes and Landforms*, 38(14), 1685–1699. doi: 10.1002/esp.3406
- Ringenbach, J. C., Pinet, N., Delteil, J., & Stephan, J. F. (1992). Analyse des structures engendrees en regime decrochant par le seisme de Nueva Ecija du 16 juillet 1990, Luzon, Philippines. *Bulletin - Societe Geologique de France*, 163(2), 109–123.
- Royden, L. H., K., C. M., & Whipple, K. X. (2000). Evolution of river elevation profiles by bedrock incision; analytical solutions for transient river profiles related to changing uplift and precipitation rates. In *Eos, transactions, american geophysical union* (Vol. 81, pp. 1–2). Fall Meeting Supplement.
- Royden, L. H., & Perron, J. (2013). Solutions of the stream power equation and application to the evolution of river longitudinal profiles. *Journal of Geophysical Research: Earth Surface*, 118(2), 497–518. doi: 10.1002/jgrf.20031
- Safran, E. B., Bierman, P. R., Aalto, R., Dunne, T., Whipple, K. X., & Caffee, M. (2005). Erosion rates driven by channel network incision in the Bolivian Andes. *Earth Surface Processes and Landforms*, 30(8), 1007–1024. doi: 10.1002/esp.1259
- Scherler, D., Bookhagen, B., & Strecker, M. R. (2014, February). Tectonic control on 10be-derived erosion rates in the Garhwal Himalaya, India. *Journal of Geophysical Research: Earth Surface*, 119(2), 83–105. doi:

- 10.1002/2013JF002955
- Schoenbohm, L. M., Whipple, K. X., Burchfiel, B. C., & Chen, L. (2004, July). Geomorphic constraints on surface uplift, exhumation, and plateau growth in the Red River region, Yunnan Province, China. *GSA Bulletin*, 116(7-8), 895–909. doi: 10.1130/B25364.1
- Seagren, E., & Schoenbohm, L. (2019). Base level and lithologic control of drainage reorganization in the sierra de las planchadas, nw argentina. *Journal of Geophysical Research: Earth Surface*, 124, 1516–1539. doi: 10.1029/2018JF004885
- Seeber, L., & Gornitz, V. (1983, March). River profiles along the Himalayan arc as indicators of active tectonics. *Tectonophysics*, 92(4), 335–367.
- Shelef, E., Haviv, I., & Goren, L. (2018, March). A potential link between waterfall recession rate and bedrock channel concavity. *Journal of Geophysical Research: Earth Surface*, 0(0). doi: 10.1002/2016JF004138
- Sklar, L., & Dietrich, W. E. (1998). River longitudinal profiles and bedrock incision models: Stream power and the influence of sediment supply. In J. Tinkler & E. Wohl (Eds.), *Geophysical Monograph Series* (Vol. 107, pp. 237–260). Washington, D. C.: American Geophysical Union. doi: 10.1029/GM107p0237
- Snyder, N. P. (2000). Landscape response to tectonic forcing: Digital elevation model analysis of stream profiles in the Mendocino triple junction region, northern California. *Geological Society of America Bulletin*, 14.
- Stock, J., & Dietrich, W. E. (2003). Valley incision by debris flows: Evidence of a topographic signature. *Water Resources Research*, 39(4). doi: 10.1029/2001WR001057
- Struth, L., Garcia-Castellanos, D., Viaplana-Muzas, M., & Vergés, J. (2019, February). Drainage network dynamics and knickpoint evolution in the Ebro and Duero basins: From endorheism to exorheism. *Geomorphology*, 327, 554–571.
- ter Borgh, M. M. (2013). *Connections between sedimentary basins during continental collision* (Unpublished doctoral dissertation). University of Utrecht.
- Tucker, G. E., & Whipple, K. X. (2002). Topographic outcomes predicted by stream erosion models: Sensitivity analysis and intermodel comparison. *Journal of Geophysical Research: Solid Earth*, 107(B9), ETG 1–1–ETG 1–16. doi: 10.1029/2001JB000162
- Turowski, J. M. (2021). Upscaling Sediment-Flux-Dependent Fluvial Bedrock Incision to Long Timescales. *Journal of Geophysical Research: Earth Surface*, 126(5), e2020JF005880. doi: 10.1029/2020JF005880
- Watkins, S. E., Whittaker, A. C., Bell, R. E., Brooke, S. A. S., Ganti, V., Gawthorpe, R. L., ... Nixon, C. W. (2020, December). Straight from the source’s mouth: Controls on field-constrained sediment export across the entire active Corinth Rift, central Greece. *Basin Research*, 32(6), 1600–1625. doi: 10.1111/bre.12444
- Whipple, K. X. (2004). Bedrock Rivers and the Geomorphology of Active Orogens. *Annual Review of Earth and Planetary Sciences*, 32(1), 151–185. doi: 10.1146/annurev.earth.32.101802.120356
- Whipple, K. X., DiBiase, R. A., & Crosby, B. T. (2013, mar). Bedrock Rivers. In *Treatise on geomorphology* (Vol. 9, pp. 550–573). Elsevier Inc. doi: 10.1016/B978-0-12-374739-6.00254-2
- Whipple, K. X., DiBiase, R. A., Ouimet, W. B., & Forte, A. M. (2017, January). Preservation or piracy: Diagnosing low-relief, high-elevation surface formation mechanisms. *Geology*, 45(1), 91–94. doi: 10.1130/G38490.1
- Whipple, K. X., & Tucker, G. E. (1999). Dynamics of the stream-power river incision model: Implications for height limits of mountain ranges, landscape response timescales, and research needs. *Journal of Geophysical Research: Solid Earth*, 104(B8), 17661–17674. doi: 10.1029/1999JB900120
- Whipple, K. X., & Tucker, G. E. (2002). Implications of sediment-flux-dependent



- river incision models for landscape evolution. *Journal of Geophysical Research: Solid Earth*, 107(B2), ETG-3.
- Whittaker, A. C. (2012). How do landscapes record tectonics and climate? *Lithosphere*, 4(2), 160–164. doi: 10.1130/RF.L003.1
- Whittaker, A. C., & Boulton, S. J. (2012). Tectonic and climatic controls on knick-point retreat rates and landscape response times. *Journal of Geophysical Research: Earth Surface*, 117(F2).
- Wickert, A. D., & Schildgen, T. F. (2019, January). Long-profile evolution of transport-limited gravel-bed rivers. *Earth Surface Dynamics*, 7(1), 17–43. doi: <https://doi.org/10.5194/esurf-7-17-2019>
- Willett, S. D. (2010). Erosion on a line. *Tectonophysics*, 484(1), 168–180. Retrieved from <https://www.sciencedirect.com/science/article/pii/S0040195109005095> (Quantitative modelling of geological processes) doi: <https://doi.org/10.1016/j.tecto.2009.09.011>
- Willett, S. D., McCoy, S. W., Perron, J. T., Goren, L., & Chen, C.-Y. (2014, March). Dynamic Reorganization of River Basins. *Science*, 343(6175), 1248765–1248765. doi: 10.1126/science.1248765
- Wobus, C. W., Crosby, B. T., & Whipple, K. X. (2006, June). Hanging valleys in fluvial systems: Controls on occurrence and implications for landscape evolution. *Journal of Geophysical Research: Earth Surface*, 111(F2), F02017. doi: 10.1029/2005JF000406
- Yin, A. (2006, May). Cenozoic tectonic evolution of the Himalayan orogen as constrained by along-strike variation of structural geometry, exhumation history, and foreland sedimentation. *Earth-Science Reviews*, 76(1), 1–131.
- Zaprowski, B. J., Pazzaglia, F. J., & Evenson, E. B. (2005). Climatic influences on profile concavity and river incision. *Journal of Geophysical Research: Earth Surface*, 110, F03004. doi: 10.1029/2004JF000138
- Zhang, Y., Hassan, M. A., King, L., Fu, X., Istanbuluoglu, E., & Wang, G. (2020). Morphometrics of China’s Loess Plateau: The spatial legacy of tectonics, climate, and loess deposition history. *Geomorphology*, 354, 107043. doi: 10.1016/j.geomorph.2020.107043